

Defect States and Polarons in Photocatalytic Semiconductors Revealed via Time-Resolved Spectroscopy

Yanjun Xu, Zhuan Wang, and Yuxiang Weng*

Cite This: <https://doi.org/10.1021/acs.jpcc.4c03688>

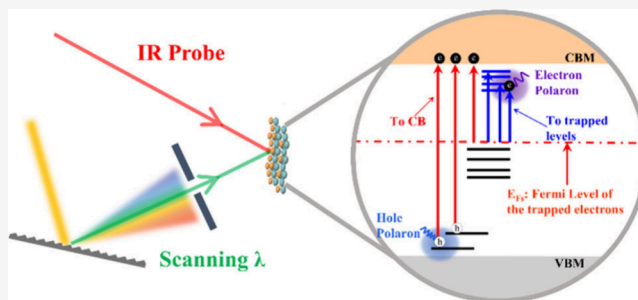
Read Online

ACCESS |

Metrics & More

Article Recommendations

ABSTRACT: Defect states and polarons of photocatalytic semiconductors play important roles by notably influencing carrier mobility and reactivity. Extensive studies have focused on identifying defect states and the physical properties of polarons, as well as their consequential impact on catalytic efficiency. This Featured Article summarizes recent investigations of defects and polarons using time-resolved spectroscopies in photocatalytic semiconductors. These include transient infrared absorption–excitation energy scanning spectroscopy to identify defect states within the bandgap of photocatalytic materials such as anatase and rutile TiO₂, ZnO, and CdS and time-resolved spectroscopic studies on the temporal evolution of photogenerated electron and hole polarons within these semiconductors. Finally, we address the current challenges in the study of defects and polarons.



Finally, we address the current challenges in the study of defects and polarons.

1. INTRODUCTION

In recent decades, remarkable progress has been made in utilizing photocatalytic semiconductor materials for applications such as solar overall water splitting to produce H₂ and O₂,¹ as well as for the degradation of pesticides, grease, and textiles in real wastewater² and sophisticated macromolecular synthesis.³ Generally, semiconductor photocatalysts are nanocrystalline, introducing various defects that act as traps for photogenerated carriers, thereby affecting photocatalytic reactions. For example, defects can serve as recombination centers for charge carriers, decreasing their lifetime,⁴ or as active sites that increase the content of surface-adsorbed products.⁵ Ideally, photocatalytic semiconductor materials are highly photoreactive in their perfect lattices,^{6,7} and several methods, such as metal ion doping,⁸ thermal annealing, solvothermal treatment,⁹ and recrystallization,¹⁰ can improve their crystallinity. For instance, aluminum cation-compensated doping in SrTiO₃ extends carrier lifetimes by passivating oxygen vacancy defects (V_O) in SrTiO₃ lattices.⁸ Later, it was recognized that defects in semiconductors can extend the visible light absorption region and enhance photocatalytic efficiency. Typical photocatalytic semiconductors such as TiO₂,¹¹ ZnO,¹² CdS,¹³ GaAs, GaP, CdSe, and SiC^{14–16} have been modified through defect engineering to enhance their photocatalytic efficiency. For example, through surface defect engineering, Shi et al. discovered that sulfur vacancy defects in P-doped CdS act as active sites on the CdS surface, prolonging the lifetime of photogenerated electrons.¹³ Shahrezaei et al. reported that V_O and Ti³⁺ species in TiO₂ nanotubes can effectively trap and stabilize Pt single-atomic catalysts, showing excellent performance in photocatalytic water

splitting.¹¹ These surface defect states act as mid-gap states located between the valence band (VB) and conduction band (CB) of semiconductors, influencing photocatalysis efficiency by trapping electrons and holes.^{14,17} In photocatalytic water splitting, the ideal energy difference between the VB and CB edges of the materials is reported as 1.6–2.4 eV,¹⁸ ensuring the two band edges must straddle the electrochemical potentials of the O₂/H₂O and H⁺/H₂ redox couples. Electrons and holes are more reducible and oxidizable, respectively, when positioned more negatively or positively than the electrochemical potential of H⁺/H₂ or O₂/H₂O.¹⁹ Trapped electrons and holes within the band gap can also participate in photocatalytic water splitting if their trapped energy levels exceed the electrochemical potential of the O₂/H₂O and H⁺/H₂ redox couples. Photocatalytic reactions primarily occur at the surface of the semiconductor materials, where the surface may have many defects. Owing to the faster relaxation rates of photogenerated free carriers to trapped states (ps to ns) compared to surface chemical reactions (ms to s),²⁰ chemical reactions proceed at trapped states rather than free-carrier states. Once photogenerated free-carrier states relax to trapped states, accompanied by phonon coupling, they form electron and hole polarons.²¹ Therefore, it is necessary to

Received: June 3, 2024

Revised: July 19, 2024

Accepted: July 19, 2024

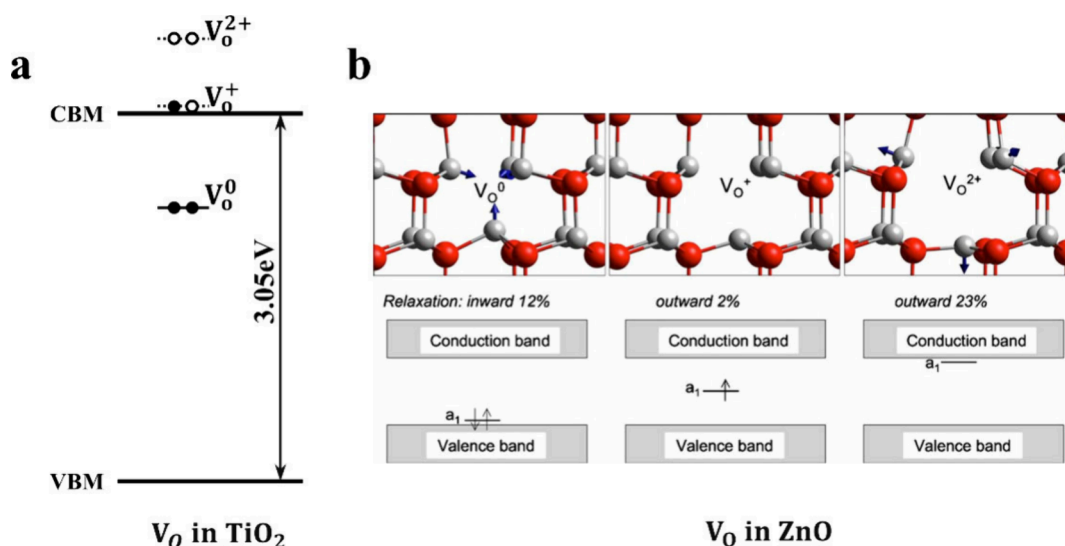


Figure 1. Position of the oxygen vacancy (V_O) in TiO_2 and ZnO . (a) Calculated energetic position of the relaxed V_O in TiO_2 .³⁷ (b) Ball-and-stick representation of the local atomic relaxations around the V_O in the 0, 1+, and 2+ charge states in ZnO . The position of the a_1 state is shown for the equilibrium configuration of each charge state.³⁸ (a) Reproduced with permission from ref 37. Copyright 2010 American Physical Society. (b) Reproduced with permission from ref 38. Copyright 2005 American Institute of Physics.

develop methods to detect the energy levels of mid-gap states and probe the formation of electron and hole polarons.

Several methods are available for detecting defect states and their trapping and recombination kinetics, including ultraviolet–visible absorption spectroscopy,²² electrochemical impedance spectroscopy,²³ photoluminescence (PL),²⁴ photoconductivity,²⁵ space charge limited current,²⁶ time-resolved X-ray absorption spectroscopy (TR-XAS)^{27,28} and visible transient absorption spectroscopy (VIS-TAS).²⁹ However, methods such as PL only provide broad spectral features, making it challenging to differentiate between trapped states and discrete states. Additionally, these methods cannot simultaneously define the initial and final states of the optical transition, complicating the alignment of the mid-gap energy levels respect to the CB minimum (CBM) or the VB maximum (VBM). In light of these challenges, we developed the transient infrared (IR) absorption–excitation energy scanning spectroscopy (TIRA–EESS) method.³⁰ TIRA–EESS accurately locates discrete defect states within the band gap of semiconductors and identifies the initial and final states of the transition process. This method distinguishes surface defects from bulk phase defects in anatase and rutile TiO_2 by comparing the mid-gap-induced transition intensity of TiO_2 nanoparticles of different sizes.³¹ It also provides information about mid-gap states in ZnO and CdS ,³² where the energy levels of point defects, such as vacancies and interstitials, can be identified in the band structure with reference to the theoretical calculations^{33–35} and a series of fluorescence experiments^{24,36} in the literature.

Typically, three types of isolated defects in semiconductors are considered: vacancies, interstitials, and anti-site defects.³⁹ The energy levels of these defects have been studied theoretically by calculating the density of states and thermodynamic transition level of defects with different charge states.^{40–42} In practical research, only defects with the lowest formation energy are usually considered. For instance, in TiO_2 , the O vacancy (V_O), with the lowest formation energy among all point defects,⁴³ forms when an O atom is removed from the TiO_2 lattice, resulting in three Ti dangling bonds pointing into the V_O .³⁷ The charge state of the V_O depends on the occupancy of

electrons within the V_O .⁴⁴ In the +2-charge state of V_O (V_O^{2+}), there is no trapped electron occupancy, causing the three nearest-neighbor Ti atoms to relax away from the vacancy, leading to a shift of the defect levels to higher energy in the CB, as shown in Figure 1(a). Conversely, in the neutral charge state (V_O^0), the V_O defect is doubly occupied by trapped electrons, with Ti atoms remaining close to their nominal positions, resulting in a gain of electronic energy and a shift to lower energy levels. The energy level of +1 charge V_O (V_O^{1+} , occupied by one trapped electron) is expected to be positioned between the V_O^{2+} and V_O^0 states near the bottom of the CB.³⁷ Similar works³⁸ have also been reported to calculate the energy levels of 0, +1 and +2 charge states of V_O in ZnO semiconductors, as presented in Figure 1(b), where the V_O of different charge states in ZnO are all located within the bandgap.

The Fermi level of the trapped states (E_{Fs}) is analogous to the quasi-Fermi levels for trapped electrons in bulk semiconductors, different from the Fermi level of free electrons (E_{Fn}), which represents the quasi-Fermi level of excess electrons in a nonthermal equilibrium semiconductor.⁴⁵ Based on this E_{Fs} concept, defects are considered filled with trapped electrons when located below the E_{Fs} , while defects without trapped electrons reside above E_{Fs} . If the electrons in the semiconductors are excited from the ground state to the excited state by the laser with different wavelengths, four types of transitions can occur when the excitation wavelength is scanned upward from the above band gap energy: (1) from VB to CB, (2) from VB to defect levels above E_{Fs} , (3) from defect levels below E_{Fs} to CB, and (4) between defect levels below and above E_{Fs} .^{30,31} Optical transitions induced by above band-gap illumination (VB to CB transition) predominantly occur from a singularity of a filled band (e.g., VBM) to a singularity of an empty band (e.g., CBM) owing to the van Hove singularity effect.⁴⁶

Excess electrons (or holes) located within lattice defects deform the highly polarizable crystal lattice and form quasiparticles known as polarons, which consist of the electrons (or holes) and an associated lattice deformation.^{47,48} The behavior of these charge carriers can be classified into three distinct types based on the strength and nature of their

interaction with the lattice: (i) free, delocalized carriers in the absence of coupling, (ii) electrons (or holes) moving within their self-induced long-range polarization cloud (large polarons) under weak coupling, and (iii) immobile self-trapped electrons (or holes) (small polarons) resulting from sufficiently strong short-range electron–phonon interaction.^{49,50} Since Landau introduced the concept of self-trapped carriers as polarons in 1933,⁴⁸ there has been increasing theoretical and experimental interest in studying polarons. In ionic, polar, and ferroelectric materials, a large polaron can typically be described using the Fröhlich polaron model, characterized by nonlocal interaction between the electron and a longitudinal optical phonon branch, as shown in Figure 2(a). The formation energy of large polarons

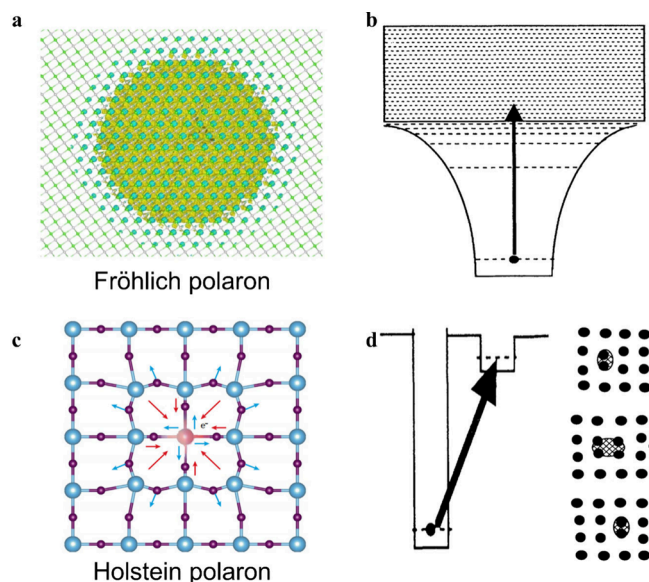


Figure 2. Schematic illustration of large and small polarons. (a) A Fröhlich-type polaron with a formation energy of 37 meV and a radius of 147 Å.⁶⁰ (b) Photoionization of a large polaron occurs when a self-trapped carrier is excited from the ground state of the potential well to the continuum of unbound states, with horizontal dashed lines representing energy levels of the bound and continuum states.²¹ (c) Schematic illustration of polarization caused by the self-trapping of an electron at a lattice site and the formation of a Holstein polaron.⁶¹ (d) (left) Schematic representation of the photoionization of a small polaron. (right) Transport of a small self-trapped carrier (hatched region) requires the motion of atoms (black dots). Incoherent motion occurs as the self-trapped carrier adjusts to the classical motion of atoms.²¹ (a) Reproduced from ref 60. Available under a CC-BY license. Copyright 2023 Hyungjun Lee et al. (b) Reproduced with permission from ref 21. Copyright 1993 American Physical Society. (c) Adapted with permission from ref 61. Copyright 2020 Wiley-VCH. (d) Reproduced with permission from ref 21. Copyright 1993 American Physical Society.

resembles those of a hydrogen atom,^{47,51} and their photoionization can be modeled using the potential well of a hydrogen atom, as shown in Figure 2(b).^{52,53} This model considers the excitation of polarons from the ground state of the self-trapping potential well to excited states within the hydrogenic potential, with higher energy capable of exciting self-trapped polarons into the continuum of free-carrier states.²¹ Sezen et al. experimentally studied the hydrogenic potential well model using infrared spectroscopy, attributing the IR absorption peaks observed at 112 meV (910 cm⁻¹), 149 meV (1205 cm⁻¹), and 170 meV (1375 cm⁻¹) to transitions from the ground state to the first,

second, and third excited states within the hydrogenic potential, respectively.⁵⁴ The radius of a large polaron is markedly larger than the lattice parameter (i.e., the distance between adjacent atoms in the lattice).⁵⁵ The effective Bohr radius of a large polaron in its hydrogenic self-trapped state is determined using $R = \frac{\hbar^2}{m^*e^2\beta}$ ²¹ where R is the effective Bohr radius of a large polaron, m^* is the carrier's band effective mass, e is the elementary charge and $\beta = \left(\frac{1}{\epsilon_\infty} - \frac{1}{\epsilon_0}\right)$, with ϵ_∞ as the high-frequency (optical) dielectric constant and ϵ_0 as the static dielectric constant of semiconductor. The effective mass of large polarons (m^*) can be approximated as $m^* \approx m\alpha^4$, where α is the dimensionless electron–phonon interaction strength and m is the mass of free electrons.^{21,47} In terms of their migration, large polarons can move similar to free particles with an effective mass of m^* if their de Broglie wavelength exceeds their radius,²¹ defined as $\lambda = \frac{\hbar}{m^*v}$, where v is the velocity of large polarons. Conversely, small polarons are characterized by the Holstein model, which considers short-range electron–phonon (optical) interactions in molecular crystals. In this model, the energy of a charge carrier depends solely on the deformation of the molecule it occupies.^{56,57} The radius of small polarons is comparable to the lattice parameter (Figure 2(c)).⁵⁵ The motion of small polarons between sites is incoherent, involving hopping processes (Figure 2(d)).⁵⁸ During this incoherent motion, a self-trapping state is destroyed at one site while simultaneously initiated at a neighboring site.^{21,59} Consequently, compared with the large polaron, small polarons exhibit lower mobility and higher effective mass. The minimum effective mass associated with coherent motion of small polaron is expressed as $m^* \approx \frac{\hbar}{R_{coh}(O)a^2}$ ²¹ where $R_{coh}(O)$ represents the maximum rate of such coherent motion occurring at absolute zero temperature,⁵⁷ and a denotes the distance of polaron movement per lattice constant.

The properties of polarons are increasingly important in photocatalytic semiconductors because the photoexcitation of polaronic states and the transport of photogenerated carriers are imperative in determining photocatalytic efficiency.^{58,62} The transport of electrons depends on the coupling mechanism of carriers with lattice ionic vibrations. For instance, Zhu et al. identified the crucial role of polarons (Ti³⁺OH) in electron storage and transfer, where the polaron states are located at the CdS–TiO₂ heterojunction interface.⁶³ Therefore, fundamental research into characterizing the transient behavior of polarons under photoexcitation is crucial for understanding their role in semiconductor properties after photoexcitation.^{64–66}

Currently, the presence of polarons in semiconductor materials can be detected through various experimental techniques, including scanning tunneling microscopy (STM),^{67,68} atomic force microscopy,⁶⁹ angle-resolved photoemission spectroscopy,⁷⁰ electron paramagnetic resonance,^{71–73} and Raman scattering.^{74–76} For instance, Guo et al. utilized a pulsed laser by coupling to the STM junction to investigate the relaxation dynamics of single polarons trapped to V_O on the surface of rutile TiO₂. They established a direct correlation between the atomic environment and the photo-response of polarons using homemade cryogenic STM.⁷⁷ However, steady-state microscopy or spectroscopy cannot capture the time-resolved formation process of polarons, specifically the coupling of excited carriers and phonons. Therefore, ultrafast spectroscopy

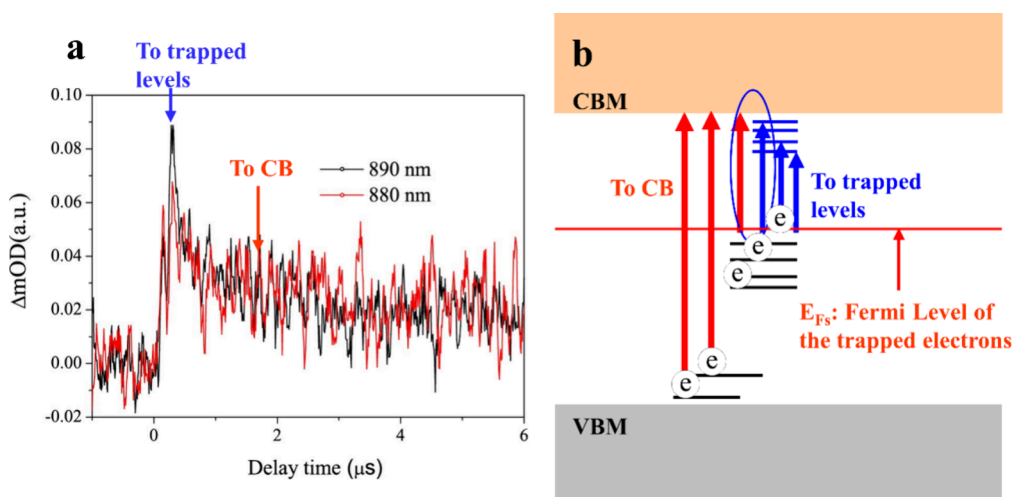


Figure 3. Determination of the Fermi level of trapped electrons (E_{Fs}). (a) Transient mid-IR decay kinetics of anatase TiO₂ excited at 880 and 890 nm, showing the critical excitation wavelength of 890 nm where a faster decay component appears. (b) Schematic illustration of the difference between electron excitation from E_{Fs} to the CB and excitation to trapped states below the CB.³⁰ (a) and (b) Reproduced from ref 30. Copyright 2013 American Chemical Society.

copy has become the mainstream technology for experimentally detecting polaron formation. Over the past decades, femto-second time-resolved spectroscopy techniques have remarkably advanced in polaron detection owing to their unique technical advantages.⁷⁸ For instance, time-resolved resonance Raman spectroscopy, sensitive to local structure and intermolecular order of crystals, provides direct insights into phonon peaks during polaron formation.^{79,80} Transient absorption spectroscopy (TAS) is another frequently utilized method for detecting polarons in various materials, including two-dimensional materials (few-layer PtSe₂),⁸¹ perovskites (MAPbI₃),⁸² photoelectric materials (hematite α -Fe₂O₃),⁸³ and core-shell CdSe/CdS nanoplatelets.⁸⁴ TAS detects excitation-induced phonons through the oscillation signal from phonons coupling to the trapped carriers in TA kinetics.

This Featured Article highlights recent developments in our laboratory in the detection of mid-gap energy levels and polaron states in photocatalytic semiconductors through TAS and TIRA-EESS. We introduce methods such as TIRA-EESS and mid-IR TAS for detecting energy levels of defects or trapped states within the bandgap, along with the kinetics of polarons. Furthermore, other related works are reviewed to shed further insights into the dynamic evolution of polarons in different photocatalytic semiconductors, including TiO₂, ZnO, and CdS. Finally, several outlooks and pending problems are summarized.

2. RESULTS AND DISCUSSION

2.1. TIRA-EESS for Detection of Mid-Gap Defects.

There are two types of TIRA-EESS based on time resolution: nanosecond time-resolved TIRA-EESS and femtosecond time-resolved TIRA-EESS. The nanosecond time-resolved TIRA-EESS was initially measured using the nanosecond time-resolved TA kinetics with scanning excitation photon energy within the bandgap of semiconductors. Specifically, a 532 nm pulse laser from an Nd:YAG laser pumped an optical parametric oscillator (OPO, Spectra-Physics), generating output wavelength ranging from 350 to 2,400 nm, which served as the wavelength-scanning excitation source for exciting the mid-gap states. A continuous mid-IR probe laser from a quantum cascade laser (4.78 μ m DRS Daylight Solutions) was employed as a

probe source and the probe light is detected by a single-channel mercury cadmium telluride (MCT) detector (Kolmar). The kinetics were recorded using a digital storage oscilloscope.^{30,31} Finally, TIRA-EESS was performed by recording the time-resolved difference absorbance against the excitation wavelength.

The TIRA-EESS involves scanning the excitation photon energy within the band gap of semiconductors, where electrons are optically excited directly into the CB or into localized unoccupied mid-gap states below the CB.⁸⁵ The transient mid-IR spectra serve as probes to differentiate various kinds of excited electrons.⁸⁶ Based on the Drude model describing the absorption spectra of electrons in the mid-IR region, its line shape can be described using the formula $\Delta OD(\lambda) \propto \lambda^p$, where the exponent p distinguishes different kinds of free electrons. Theoretical values of p are 1.5, 2.5, and 3.5 for free electrons scattered by acoustic phonons, optical phonons, and ionized impurities, respectively.^{86,87} In addition, as the lifetimes of electrons in the CB and trapped states differ, their final states can be recognized by their respective kinetics.³⁰ This characteristic feature has been used to determine E_{Fs} at the turning point of photogenerated electron decay kinetics. Figure 3(a) shows the kinetics of excited electrons in anatase TiO₂, where electrons excited in the CB at 880 nm exhibit slower decay kinetics, whereas those excited into trapped levels below the CBM at 890 nm decay faster.³¹ The accelerated decay kinetics is attributed to trapping by mid-gap levels. Figure 3(b) illustrates that the position of E_{Fs} in anatase TiO₂ is determined to be 1.41 eV (880 nm) below the CB. Thus, when the excitation wavelength is scanned from the above band gap transition, it is expected to identify two kinds of final states of electron transition, i.e., the electrons in CB and electrons trapped in localized states, where the two final states are expected to corresponding to two minimal transition energies: (1) from E_{Fs} to CBM and (2) from E_{Fs} to the lowest energy level of localized states.³⁰ During the search for these two minimal excitation energies, a transition in the kinetic can be observed, which appears when the excitation wavelength is less than the minimal transition energies for electron transition from E_{Fs} to CBM.³¹ Consequently, the initial

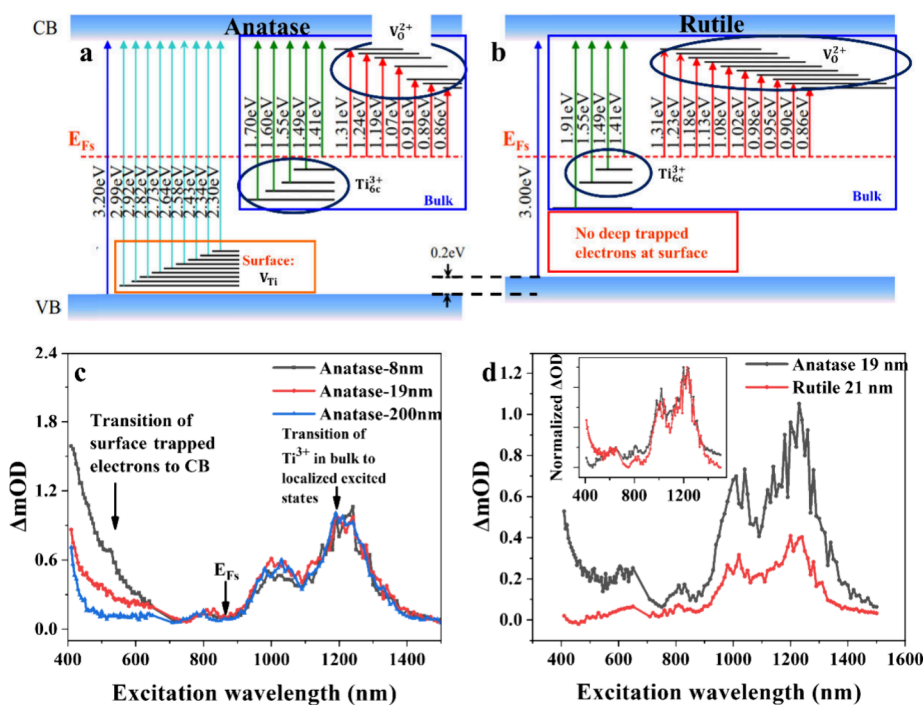


Figure 4. Experimentally determined mid-gap energy levels via the transient infrared (IR) absorption–excitation energy scanning spectroscopy (TIRA–EESS). (a) and (b) Schematic illustrations summarizing the experimentally observed defect levels of anatase and rutile TiO_2 nanoparticles, respectively. (c) TIRA–EESS results for anatase nanoparticles of three different sizes (8, 19, and 200 nm), distinguishing between surface and bulk defects. (d) TIRA–EESS comparison between anatase and rutile nanoparticles of similar size (~ 20 nm), with the inset showing the corresponding normalized spectra. Anatase exhibits a much higher density of both the surface and bulk defects compared to rutile.³¹ (a–d) Adapted from ref 31. Available under a CC-BY license. Copyright 2015 Yang Mi et al.

states of excitation can be determined based on the position of final states, E_{Fs} , and the excitation wavelength.

Femtosecond time-resolved TIRA–EESS was measured using a femtosecond TA spectrometer equipped with a titanium-doped sapphire laser as the light source. The laser output was divided into two beams: one beam pumped an optical parametric amplifier (OPA) to provide tunable narrow-band excitation wavelengths from ultraviolet (300 nm) to mid-infrared (6,000 nm), serving as a wavelength-scanning excitation source for mid-gap states. The other beam generated mid-infrared supercontinuum light (3–10 μm) through four-wave mixing in air, used as a probe to detect the excited electrons. The probe light was focused into a monochromator and detected through a 64-channel MCT array detector (Infrared Systems Development) with a spectral resolution of 10 nm. Femtosecond TIRA–EESS data were also recorded to show the difference in absorbance against the excitation wavelength. The IR absorbance was normalized by the excitation intensity, quantified in terms of the photon number.

Compared to nanosecond TIRA–EESS, femtosecond TIRA–EESS offers three advantages: (1) higher temporal resolution: nanosecond TIRA–EESS is limited by the response time of the MCT detector (80 ns), while femtosecond TIRA–EESS achieves a resolution of 100 fs. (2) Broad detection spectral region: the 64-channel MCT detector covers a wide spectrum from 3 to 10 μm with a spectral resolution of 10 nm. (3) Broad excitation wavelength region: nanosecond TIRA–EESS uses an OPO with a scanning wavelength excitation range of 350–2400 nm, while femtosecond TIRA–EESS uses an OPA, covering 300 to 6000 nm. The extension of excitation wavelength into the mid-IR region allows the femtosecond TIRA–EESS to detect shallow trapped states. However,

nanosecond TIRA–EESS observe kinetics ranging from 100 ns to 10 ms, while femtosecond TIRA–EESS is limited to 3 ns.

2.2. Detection of Defect States via TIRA–EESS in Photocatalytic Materials. TIRA–EESS provides the energy levels of mid-gap states in bandgap of semiconductors with nanosecond or femtosecond time resolution. We will briefly review the determination of mid-gap energy levels and excited polarons via TIRA–EESS and TAS in several typical semiconductor photocatalytic materials.

2.2.1. TiO_2 . TiO_2 is a wide band gap (3.2 eV) oxide semiconductor, a widely studied material for photocatalysis and solar energy conversion.⁸⁸ TiO_2 exists in three common crystalline structures: anatase, rutile, and brookite. Generally, anatase TiO_2 is recognized as the most active phase in photocatalysts for environmental applications, while only rutile TiO_2 can proceed photocatalytic overall water splitting. Surface defects engineering is pivotal for improving the photocatalytic efficiency of TiO_2 , modifying its surface properties and band structure.⁸⁸ V_O is the most common defects in TiO_2 owing to their lowest formation energy compared to other defects.⁸⁹ The formation of V_O involves the removal of a neutral oxygen atom, resulting in excess electrons occupying the vacant Ti sites and the generation of Ti^{3+} species.⁹⁰ These defects play an important role in several processes of photocatalysis. For example, the defects of Ti^{3+} act as color centers that enable visible light absorption, and surface defects can also serve as active sites for photocatalytic redox reactions.⁹¹ The difference in photocatalytic efficiency between anatase and rutile TiO_2 can be attributed to the distinct defect levels detected via TIRA–EESS.

Zhu and co-workers proposed the nanosecond TIRA–EESS method in 2013,³⁰ employing it for the accurate determination of mid-gap energy levels in anatase TiO_2 (Figure 4(a)). They

achieved an energy resolution of 0.02 eV. They reported over 20 occupied trapped states below the E_{F_s} across an excitation wavelength range of 400 to 880 nm, and seven unoccupied states below the CB in a range from 890 to 1400 nm in anatase TiO₂ nanoparticles with an average size of 7.9 nm. The E_{F_s} was determined to be 1.41 eV below the bottom of CB. In a follow-up study,³¹ the same method was applied to further detect the mid-gap energy levels in rutile TiO₂ nanoparticles (Figure 4(b)), revealing ten unoccupied states below the CB in the near-infrared (NIR) range and three occupied trapped states below the E_{F_s} in the visible range. Moreover, they differentiated surface defect states and bulk defect states (specifically the 6-fold coordinated Ti_{6c}³⁺ site⁹²) in anatase TiO₂ by detecting mid-gap states across anatase TiO₂ nanoparticles of different sizes (Figure 4(c)). Surface defect states are deeply trapped, located between 2.30 and 2.99 eV below the bottom of the CB, while bulk phase defects (i.e., Ti_{6c}³⁺ defects) represent shallower trapped states located from 1.41 to 1.70 eV below the bottom of the CB. Figure 4(d) compares TIRA–EESS results of anatase and rutile TiO₂ of similar sizes around 20 nm. In the visible region (400 to 500 nm), corresponding to the transition of surface-trapped electrons to CB, rutile nanoparticles exhibit negligible surface-trapped states compared to anatase. This observation indicates that anatase exhibits a greater abundance of surface defects suitable for chemical adsorption, whereas rutile fewer surface defects and fewer bulk defects than anatase. The transitions of shallow trapped states in the bulk to localized excited states appear in the NIR region (890 to 1400 nm), exhibiting a strikingly similar spectral line shape in both anatase and rutile TiO₂, as shown in the inset of Figure 4(d). This spectral feature serves as a reference energy ladder for assisting the band alignment of rutile and anatase. It confirms that their CBs are aligned within an uncertainty of kT ($1kT = 25$ meV at $T = 300$ K). This alignment is later confirmed via Kelvin probe force microscopy, indicating that the surface work function of rutile is 30 meV higher than that of anatase.⁹³

The measured mid-gap energy levels of anatase TiO₂, comprising 20 occupied trapped states below the E_{F_s} and seven unoccupied local states above E_{F_s} , can be categorized into three types of defect states. These include shallow empty defect states near the CBM in the bulk (ranging from 0.86 to 1.31 eV above E_{F_s}), electron-filled defect states below the E_{F_s} in the bulk (ranging from 1.41 to 1.71 eV below the CBM), and electron-filled defect states near the VBM on the surface (ranging from 2.30 to 2.99 eV below the CBM). Theoretical calculations indicate that the most common defects in anatase and rutile TiO₂ are V_O and Ti³⁺. Density functional theory (DFT) on rutile TiO₂(110) surfaces demonstrated that the 6-fold-coordinated Ti_{6c}³⁺ site located with an energy of 1.6 eV below the conduction band,^{28,62} while V_O acts as shallow states below the CBM.^{33,34} Studies of PL spectra of TiO₂^{94,95} have suggested that doubly ionized V_O (V_O²⁺) in the bulk are positioned close to the CB, corresponding to the shallow empty defect states. The filled defect states just below the E_{F_s} can be assigned to Ti³⁺ in the bulk. Based on these density functional theories above, the shallow empty defect states near the CBM in the bulk (ranging from 0.86 to 1.31 eV above E_{F_s}) can be associated with V_O²⁺, while the filled defect states below the E_{F_s} in the bulk (ranging from 1.41 to 1.71 eV below the CBM) can be attributed to Ti³⁺. These two defects in the bulk have been observed in both anatase and rutile TiO₂.

In contrast, filled defect states near the VBM have been observed only on the surface of anatase TiO₂. These filled states near the VBM may originate from two sources. First, they could be attributed to Ti vacancies (V_{Ti}),^{96,97} where V_{Ti} can introduce excess free holes into the VB of TiO₂, leaving electrons located at V_{Ti} energy levels, thus altering the conductivity of TiO₂ from n-type to p-type.⁹⁸ Second, electronic structure calculations using hybrid functional methods have revealed that defects associated with hole-trapping sites typically correspond to 2-fold coordinated O_{2c}⁻ surface atoms or isolated hydroxyl (OH) species on hydroxylated surfaces, specifically terminal hydroxyl groups (OH_t).⁹⁹ When extra holes are introduced into the VB of TiO₂, 94% of the hole density becomes trapped at bridging oxygen O_{2c}⁻, resulting in substantially elongated Ti–O_{2c}–Ti bonds. However, the precise origin of these filled defect states near the VBM on the surface of anatase TiO₂—whether from V_{Ti}, O_{2c}⁻, or OH_t—remains unproven through ultrafast spectroscopy and necessitates further investigation to provide conclusive evidence.

The distribution of mid-gap states differ between anatase and rutile TiO₂, accounting for their distinct photocatalytic activities in water-splitting reactions. Rutile can proceed overall water splitting, while anatase can only produce H₂. This disparity arises because anatase TiO₂ contains a considerable number of deep trapped states located 0.6 eV above the VBM, which reduces the oxidation ability of trapped photogenerated holes. In contrast, rutile TiO₂ exhibits negligible deep trapped states. Li et al. (2015)¹⁰⁰ found that prolonged ultraviolet (UV) irradiation can transform anatase TiO₂ to facilitate overall water splitting. They employed TIRA–EESS to elucidate the difference in the mid-gap energy levels after prolonged UV irradiation. They found that the deep trapped states above the VBM can be removed via UV irradiation, rendering anatase TiO₂ the capability of water oxidation. Du et al.¹⁰¹ investigated the effects of boron (B) doping on the surface defects of anatase TiO₂ nanoparticles. They discovered that B-doped anatase surfaces exhibit enhanced O₂ generation (4.5 times improved compared with B-free surface anatase). The corresponding TIRA–EESS for B-free and B-doped surfaces of anatase nanoparticles suggested a high density of trapped states near the VBM in B-free surfaces of TiO₂. This absence of trapped states in B-doped surfaces of TiO₂ enhances the photocatalytic oxidation capability of holes, facilitating the water oxidation reaction. In summary, these studies establish a relationship between photocatalytic efficiency and defect state energy levels, revealing TIRA–EESS as a useful tool for investigating the activity of photocatalytic semiconductor materials and guiding surface defect engineering strategies.

2.2.2. ZnO and CdS. ZnO, a transition metal oxide, finds wide application in various fields owing to its economic viability, low toxicity, ease of synthesis, and modifiability.^{103,104} These applications include field effect transistors,¹⁰⁵ gas sensing layers,¹⁰⁶ dye-sensitized solar cell devices,¹⁰⁷ luminescence,¹⁰⁸ bioimaging,¹⁰⁹ and photocatalysis. To improve photocatalytic efficiency, noble metal cocatalysts, such as Ag, Au, and Pt nanoparticles, are deposited onto ZnO surfaces. These metal–semiconductor heterojunctions facilitate charge separation of electrons and holes at the heterojunction interface, thereby improving photocatalytic activity. Specifically, the photocatalytic efficiency of ZnO is markedly improved after the deposition of Ag and Au cocatalysts, while Pt cocatalyst deposition yields only marginal improvements under similar conditions.^{110,111} The mechanism by which metal–semi-

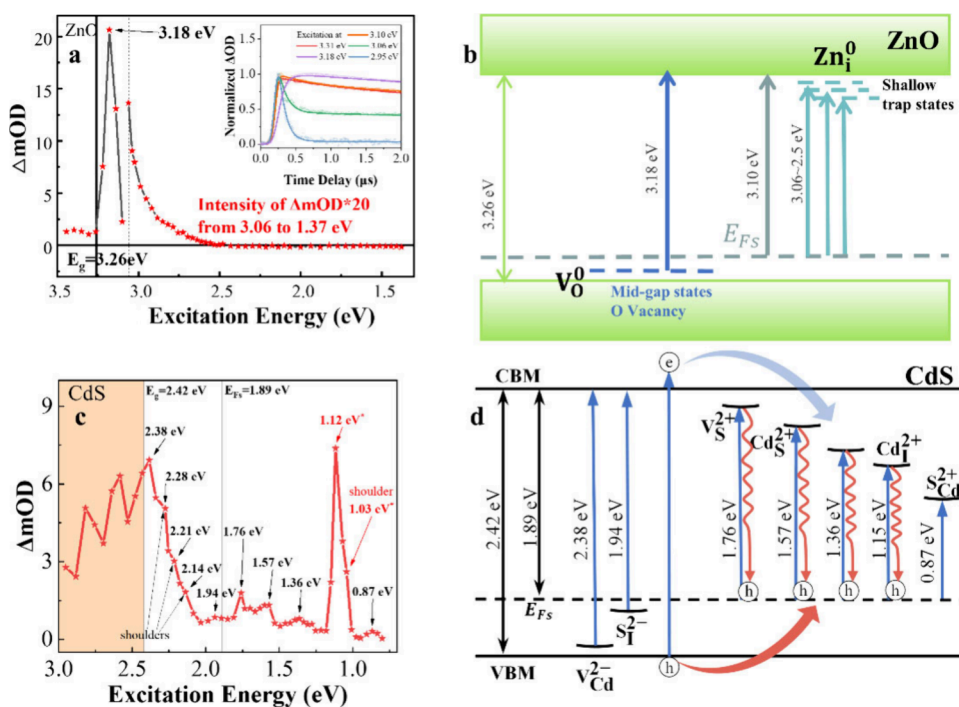


Figure 5. TIRA–EESS and the corresponding mid-gap energy diagram of defects for ZnO and CdS single crystals. (a) TIRA–EESS of ZnO single crystal probed at $4.75\ \mu\text{m}$, with insets showing kinetics probed at $4.75\ \mu\text{m}$ and excited at 3.31, 3.18, 3.10, 3.06, and 2.95 eV. (b) Schematic illustration of experimentally determined defect levels for ZnO single crystal.¹⁰² (c) TIRA–EESS of CdS single crystal probed at $5\ \mu\text{m}$. (d) Schematic illustration of experimentally determined defect levels for CdS single crystal.³² (a, b) Reproduced from ref 102. Copyright 2021 Qianxia Liu. (c, d) Reproduced from ref 32. Copyright 2024 American Chemical Society.

conductor heterojunctions promote carrier transport needs to be further explored.

Liu et al. acquired nanosecond time-resolved TIRA–EESS of ZnO single crystal, as depicted in Figure 5(a),¹⁰² with excitation energy ranging from 1.37 to 3.44 eV. The spectrum shows a prominent peak at 3.18 eV, which diminishes as excitation energy drops below 2.5 eV, aligning with the band gap of ZnO at 3.26 eV.¹¹² Thus, the observed peak at 3.18 eV likely corresponds to the transition of mid-gap states. The inset of Figure 5(a) displays decay kinetics excited at 3.31, 3.18, 3.10, 3.06, and 2.95 eV. Slower decay kinetics are observed at excitation energies of 3.10 eV and above, while faster decay occurs below 3.10 eV, suggesting the position of E_{FS} to be 3.10 eV below CBM. The mapping of TIRA–EESS data is depicted in the mid-gap energy diagram in Figure 5(b), illustrating two types of mid-gap states in ZnO single crystals: a deep trapped state at 3.18 eV below CBM and continuous shallow trap states ranging from 3.06 to 2.5 eV above E_{FS} . Considering defects in ZnO related to these mid-gap states, neutral V_O is the most probable deep defects in undoped ZnO owing to its low formation energy, whose energy level is located in the bandgap.^{113,114} Experimental data indicate three types of V_O : doubly ionized V_O (V_O^{2+}), singly ionized V_O (V_O^{1+}), and the neutral V_O (V_O^0), positioned at 0.59, 0.89, and 2 eV below CBM, respectively, supported by visible PL spectra¹¹⁵ and calculation.³⁸ Time-resolved X-ray spectroscopy also reported the ultrafast trapping of holes at V_O^{1+} sites ($<1.4\ \text{ps}$), with an outward displacement by $\sim 15\%$ of the four surrounding zinc atoms away from the V_O ,^{116,117} further demonstrating that O vacancies, as hole trapping sites, lie below the E_{FS} . Additionally, another study has assigned positions of Zn interstitial (Zn_i) and V_O at 0.22 and 1.85 eV below CBM, respectively, also through PL spectra.¹¹⁸

Consequently, the deep trapped states at 3.18 eV below CBM are likely attributed to neutral V_O (V_O^0), while the continuous shallow trap states between 3.06 and 2.5 eV above E_{FS} can be assigned to Zn_i .

CdS, a photocatalyst, preferentially activates carbon–hydrogen (C–H) bonds via photoexcited holes, facilitating highly selective carbon–carbon (C–C) coupling and diversifying available multi-carbon materials.¹¹⁹ These chemical reactions are largely related to the defects on the semiconductor surface, where defect-trapped carriers are easily coupled with phonons forming polarons, thus affecting the quantum efficiency of selective C–C coupling. For instance, Utterback et al. revealed that energetically trapped holes exhibit mobility on the surfaces of CdS nanorods over nanosecond to tens of microsecond time scales using TAS and theoretical modeling.¹²⁰ Building on this, Cline et al. proposed a model of small hole polaron hopping on sulfur atom orbitals on the CdS surface using density functional theory.¹²¹ However, experimental observation of polarons in CdS remains limited. By combining visible, NIR, mid-IR TAS, and TIRA–EESS, we can elucidate the formation and recombination kinetics of electron and hole polarons in CdS.

In 2024, Xu et al. investigated the mid-gap states and polarons in CdS single crystal using femtosecond time-resolved TIRA–EESS along with visible, NIR, and mid-IR TAS. Figure 5(c) shows the femtosecond time-resolved TIRA–EESS for CdS single crystals, revealing that the E_{FS} in CdS is located at 1.89 eV below the CBM. The spectrum shows two mid-gap states below E_{FS} (peaks at 2.38 and 1.94 eV shown in Figure 5(c)) occupied by trapped electrons, while five mid-gap states above E_{FS} (at 1.76, 1.57, 1.36, 1.12, and 0.87 eV) remain unoccupied. Based on previous experimental and theoretical research on CdS defects,^{40,42,122–124} these seven discrete energy levels can be

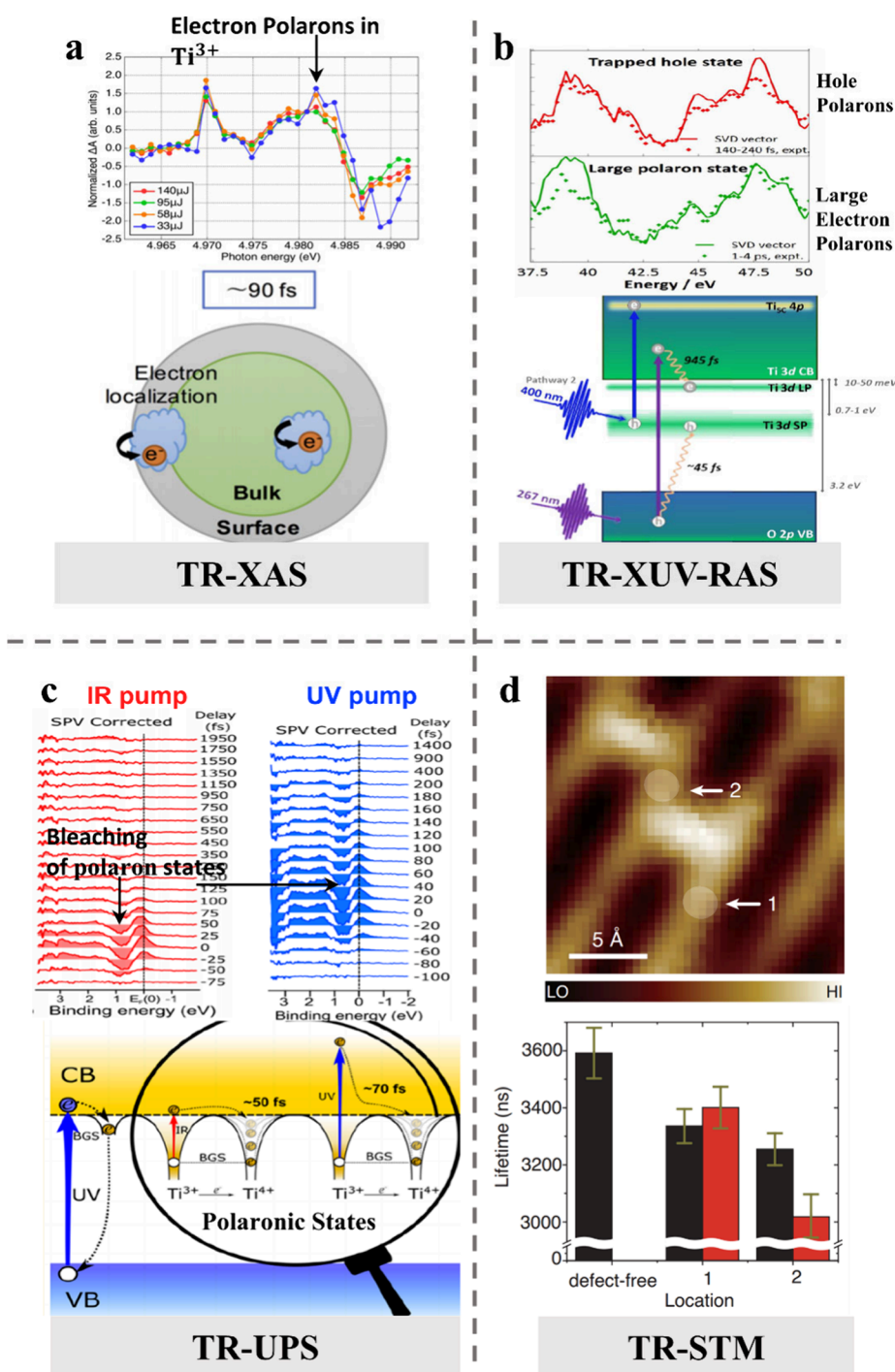


Figure 6. Electron polarons in anatase TiO_2 detected via various methods. (a) Time-resolved X-ray absorption spectroscopy (TR-XAS) of electron polarons in anatase TiO_2 nanoparticles. Top panel: normalized TR-XAS spectra of anatase TiO_2 nanoparticles excited at 268 nm with varied excitation energies, as indicated. Bottom panel: schematic illustration of electron location dynamics in anatase TiO_2 nanoparticles.¹³¹ (b) Probed hole polarons in anatase TiO_2 containing V_O using time-resolved extreme ultraviolet-reflection absorption spectroscopy (TR-XUV-RAS). Top panel: spectral components obtained via singular value decomposition (solid lines) and experimental transient spectra (dots) at various time delays following 267 nm excitation for hole and electron polarons, respectively. Bottom panel: proposed mechanism of charge relaxation and polaron formation in anatase TiO_2 after 267 and 400 nm photoexcitation.⁶⁶ (c) Retrapping of electron polarons in rutile TiO_2 single crystal detected via time-resolved ultraviolet photoelectron spectroscopy (TR-UPS). Top panel: TR-UPS ($h\nu = 20.9$ eV) measured at different delay times with IR and UV pump. Bottom panel: schematic illustration of the electron retrapping from the polaronic states within the band gap of rutile TiO_2 .¹³² (d) Lifetime characterization of electron polarons around V_O on the rutile $\text{TiO}_2(110)$ surface using time-resolved scanning tunneling microscopy (TR-STM). Top panel: topography image of a $\text{V}_\text{O}^{\text{surf}}$ dimer. Filled circles denote the positions of two ground-state polarons, where polaron 1 is isolated and polaron 2 is bound to two defects. Bottom panel: location dependence of the lifetimes for photoexcited electrons and polarons, with error bars indicating fitting errors.⁷⁷ (a) Reproduced from ref 131. Available under a CC-BY license. Copyright 2017 Yuki Obara et al. (b) Reproduced from ref 66. Copyright 2022 American Chemical Society. (c) Reproduced from ref 132. Copyright 2019 American Chemical Society. (d) Reproduced with permission from ref 77. Copyright 2020 American Physical Society.

assigned to three types of isolated defects in CdS: vacancies (Cd vacancy: V_{Cd} and S vacancy: V_S), interstitials (Cd interstitial: Cd_i and S interstitial: S_i), and anti-site (Cd atoms substituted by S atoms: S_{Cd} and S atoms substituted by Cd atoms: Cd_S).⁴⁰ These defects are arranged in ascending order of formation energy: $V_S^{2+} < Cd_i^{2+} < Cd_S^{2+} < V_{Cd}^{2-} < S_i^{2-} < S_{Cd}^{2+}$.¹²² Defects in the positively charged state are located above E_{F_s} , trapping photogenerated electrons, while defects in the negatively charged state are located below E_{F_s} , trapping photogenerated holes. There are two possible defects located below E_{F_s} : V_{Cd}^{2-} with the energy level of 0.16 eV above VBM and S_i^{2-} with 0.42 eV above VBM, as calculated by Xu et al.¹²³ Therefore, the peaks observed at 2.38 and 1.94 eV correspond to electron transitions from Cd vacancies and S interstitials to CBM, respectively. According to previously reported temperature-dependent PL kinetics of the midgap trapped states for CdS nanobelts,¹²³ four possible defects located above E_{F_s} with energy levels of 0.1, 0.5, 0.82, and 1.0 eV below CBM can be assigned to V_S^{2+} , Cd_i^{2+} , Cd_S^{2+} , and S_{Cd}^{2+} , respectively. With E_{F_s} determined at 1.89 eV below the CBM, in the mid-gap energy diagram, the defects V_S^{2+} , Cd_S^{2+} , Cd_i^{2+} , and S_{Cd}^{2+} can be assigned as final states with transition energy of 1.76, 1.57, 1.15, and 0.87 eV from E_{F_s} , respectively, as shown in Figure 5(d), while the other two defect states (2.38 and 1.94 eV below CB) can be attributed to V_{Cd}^{2-} and S_i^{2-} , respectively. We noted that for nanocrystals as quantum dots, the PL midgap surface states are coupled to the band-edge core exciton with a thermal activable barrier, unlike those without barrier described in Figure 5d.^{125,126} In addition, the peak observed at 1.12 eV in TIRA–EESS, exhibiting the highest intensity, is experimentally determined as a three-photon absorption process, with its physical origin requiring further exploration.³²

2.3. Observation of Temporal Evolution of Electron and Hole Polarons. TiO_2 consists of nominal Ti^{4+} and O^{2-} valence states. However, the unavoidable removal of surface oxygen atoms results in the emergence of two types of defects: V_O and Ti^{3+} species. The presence of additional V_O and Ti^{3+} species can generate polaron states, which exhibit distinct behavior in anatase and rutile TiO_2 . Various reviews have extensively introduced steady polaron states in both anatase and rutile TiO_2 .^{47,127} Specifically, in rutile, polarons tend to appear as small (or Holstein) polarons¹²⁸ localized at V_O , where the surrounding ions screen the trapped electrons or holes, leading to the formation of a potential well. UV photoemission spectroscopy studies have reported strongly self-trapped electron polarons with a binding energy of 1.0 eV below the Fermi level in rutile. These small electron polarons in rutile have a low-energy barrier (~ 95 meV) for phonon-assisted hopping to adjacent Ti ions, contributing to their conductivity.¹²⁹ Conversely, electron polarons in anatase TiO_2 exhibit more complex behavior compared to rutile TiO_2 . Small polarons in anatase are observed on surface defects, with a higher energy barrier for their hopping between adjacent atoms, resulting in their entrapment at the defect site. Moreover, large (or Fröhlich) polarons can appear in anatase when excess electrons are introduced through doping, causing minimal lattice distortion. These polarons are delocalized over several ions and behave as shallow states located at 40 meV below the CB, exhibiting free carrier-like properties. For instance, STM studies by Setvin et al., combined with simulation studies, reported the observation of large (or Fröhlich) polarons in the bulk phase of anatase TiO_2 ,

where they are delocalized over several ions with a size of 12–25 Å, exhibiting free carrier-like properties.^{128,130}

Santomauero et al.¹³³ and Obara et al.¹³¹ employed femto-second time-resolved Ti K-edge X-ray absorption spectroscopy to investigate the kinetics of excited polarons in anatase TiO_2 nanoparticles upon 355 and 268 nm excitation, respectively. Specifically, they demonstrated that excited electrons in anatase TiO_2 nanoparticles were predominantly trapped by penta-coordinated Ti^{3+} (Ti_{5c}^{3+}) centers on the surface region within 170 fs¹³³ or 90 fs,¹³¹ resulting in the formation of polarons located at Ti^{3+} centers (as depicted in Figure 6(a, top) with a positive band at 4.9815 eV). Both studies highlighted the presence of small electron polarons trapped at Ti^{3+} defects on the surface of anatase TiO_2 , forming within 90 to 170 fs. The formation time of electron polarons suggests a diffusion length of ~ 4.0 Å for electrons from generation to trapping, indicating their localization within or near the unit cell where they were generated. This may correspond to the high energy barrier for the migration of small electron polarons in anatase TiO_2 .

While most studies focused on electron polarons, Hruska and colleagues reported the experimental observation of hole polarons in V_O -rich anatase TiO_2 using time-resolved extreme ultraviolet-reflection absorption spectroscopy (TR-XUV-RAS) upon 267 nm excitation in 2015.⁶⁶ The spectral features of trapped hole polarons (red curves) and large electron polarons (green curves) are shown in Figure 6(b, top). Specifically, direct interband transitions with the above bandgap excitations generate hot electrons in the CB and holes in the VB, leading to the trapping of hot holes to deep V_O as small hole polarons within 45 ± 42 fs and the trapping of hot electrons at shallow V_O as large electron polarons within 945 ± 92 fs, as illustrated in Figure 6(b, bottom).

Regarding polarons in rutile TiO_2 , Zhang et al. conducted TR-UPS to examine the retrapping process of photoexcited polarons in a rutile TiO_2 single crystal.¹³² Under infrared (IR, 0.95 eV) excitation, electrons from polaron states (Ti^{3+} defect states) approximately 0.8 eV below CBM were excited to CBM, as depicted by the red arrow in Figure 6(c, bottom). The rapid retrapping of hot electrons occurs within 45 fs, much faster than the electrons excited by interband transitions (with lifetimes typically in the order of ps to ns¹³⁴). Conversely, under ultraviolet (UV, 3.5 eV) excitation, electrons can also be excited from the polaron states to the resonance state within the CB, as illustrated by the blue arrow in Figure 6(c, bottom), in addition to direct interband transitions. Interestingly, hot electrons in the CB excited by UV light predominantly originate from polaronic states, exhibiting an extremely fast retrapping lifetime of ~ 70 fs. This suggests that the density of states in the VB is not markedly higher than that of the polaron states, implying that polarons might contribute more photoexcited charge carriers than VB states under band gap excitation.¹³²

Besides spectroscopy, time-resolved STM provides valuable insights into the interaction of polarons with lattice defects. For instance, Guo et al. made progress in elucidating the kinetics of polarons trapped at V_O on the surface of rutile TiO_2 (110) using a pulsed laser-combined STM and spectroscopy.⁷⁷ Their findings revealed that the trapping time of polarons substantially decreased when the polaron was positioned at two surface V_O compared to one vacancy, as shown in Figure 6(d). This result suggests a strong correlation between surface V_O and polaron formation, indicating that shared polarons trapped around two surface V_O could exhibit enhanced catalytic activity.

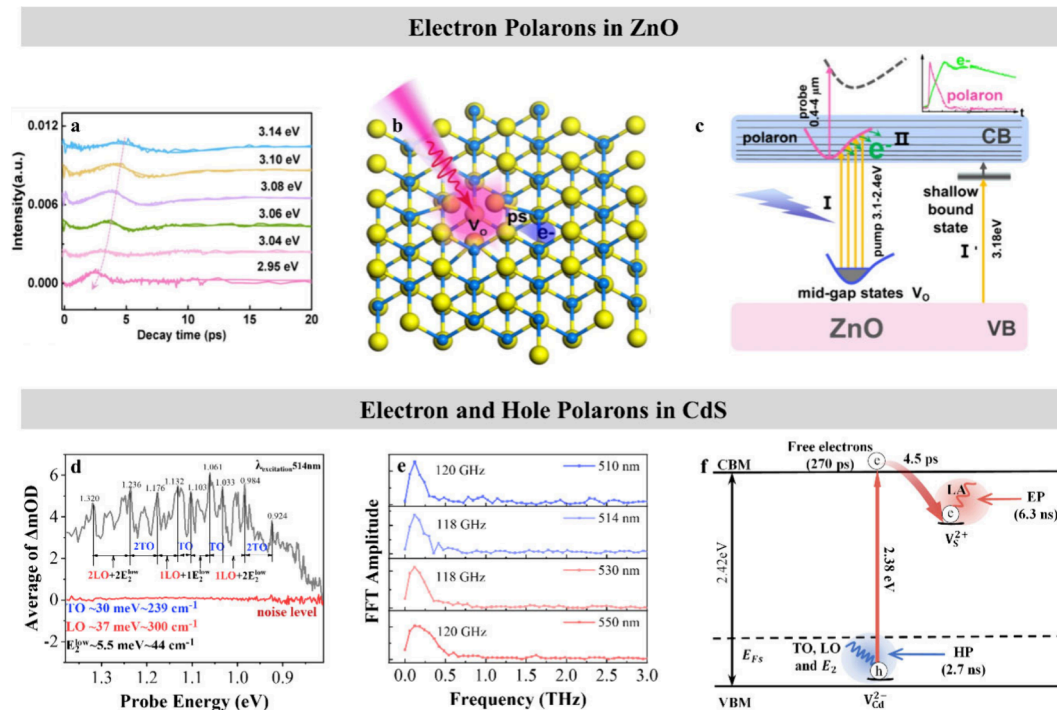


Figure 7. Polarons detected via time-resolved TAS in ZnO and CdS. (a) Phonon oscillation extracted from kinetics probed at 5 μm after excitation with energies ranging from 3.14 to 2.95 eV. (b) Schematic diagram showing polaron excitation from V_{O} via ultrafast laser and subsequent release of free electrons in ZnO single crystal. (c) Diagram representing mid-gap states of V_{O} , excited polaron, and shallow bound states in ZnO single crystal.¹¹² (d) Spectrum of hole polarons excited at 514 nm, where the energy difference between two adjacent sharp peaks matches the energy of optical phonons observed in the Raman spectrum of CdS single crystal. (e) Frequency of acoustic phonon signal extracted from kinetics probed at 5 μm after excitation with wavelengths from 510 to 550 nm. (f) Schematic illustration of processes for generating electron and hole polaron states in CdS single crystal. EP: electron polarons; HP: hole polarons; LA: longitudinal acoustic phonons; LO: LO phonon; TO: transverse optical phonon; and E_2 symmetry Raman modes.³² (a–c) Reprinted from ref 112. Copyright 2021 American Chemical Society. (d–f) Adapted from ref 32. Copyright 2024 American Chemical Society.

In 2021, Liu demonstrated the detection of excited electron polarons in ZnO single crystal using MIR-TAS, as depicted in Figure 7(a–c).¹¹² Figure 7(a) displays oscillations with a frequency of ~ 50 GHz superimposed on the kinetics probe at 5 μm while scanning the mid-gap excitation energy from 3.14 to 2.95 eV. These oscillations correspond to coherent acoustic phonons resulting from the relaxation of polaron states. The kinetics revealed that electron transfer from the excited polaron states to the CB occurs within ~ 1 ps. The entire process of polaron excitation is schematically illustrated in Figure 7(b, c). Specifically, within the excitation energy range of 3.14 to 2.95 eV, electrons trapped in V_{O} are excited to the polaron states within the CB. The excited polaronic states inject electrons into the CB within ~ 1 ps, after which the electrons become trapped and subsequently recombine with holes with a time constant of several nanoseconds. The extended lifetime of carriers from polaron excitation compared to band gap excitation confers an advantage in the photocatalytic process for ZnO. Notably, the lifetime of carriers from the polarons in rutile TiO_2 is ~ 45 fs,¹³² substantially shorter than that from band gap excitation (several nanoseconds¹³⁴). The effect of polaron excitation on carrier lifetime in ZnO and TiO_2 is diametrically different, which inspires further study on the mechanism that underlies the prolongation of carrier lifetime by polarons.

To investigate the evolution of hole polarons in typical photocatalytic semiconductors, Xu et al. utilized femtosecond time-resolved infrared TAS to identify electron and hole polarons in CdS single crystal.³² In Figure 7(d), the transient NIR spectrum generated by mid-gap excitations at 514 nm

reveals a broad absorption band ranging from 0.95 to 1.35 eV, attributed to the absorption of trapped holes. Moreover, this spectrum displays a unique line shape characterized by a series of subpeaks with intensities considerably surpassing the background baseline indicated by the red line. Notably, the energy differences between adjacent subpeaks measure 84, 60, 44, 29, 42, 28, 49, and 60 meV, consistent with the optical phonons of CdS. Specifically, 60 meV corresponds to two transverse optical modes (2TO), 42 and 44 meV correspond to one longitudinal optical mode, and one low-energy E_2 symmetry mode (1LO + 1 E_2^{low}), 84 meV corresponds to 2LO + 2 E_2^{low} , and 28 and 29 meV correspond to one transverse optical (1TO) mode. Consequently, the subpeaks observed in the transient NIR spectrum are associated with the interaction between trapped holes and optical phonons, indicating the formation of hole polarons. The 514 nm excitations induce the transition of electrons from Cd vacancies to the CBM, thereby leaving trapped holes at the Cd vacancies. This reasonably infers that hole polarons in the CdS single crystal form at Cd vacancies. Furthermore, the study reported the existence of electron polarons in the CdS single crystal through transient mid-IR absorption spectroscopy, similar to the electron polarons in ZnO. As shown in Figure 7(e), the fast Fourier transform analysis of the oscillation signal in the free-carrier decay kinetics reveals a frequency of ~ 120 GHz, matching the longitudinal acoustic (LA) phonons in CdS identified via Brillouin scattering.^{135–137} This finding validates the coupling between trapped electrons and LA phonons, indicative of electron polaron formation. The duration of

electron polaron formation is estimated to be within 4.5 ps, corresponding to electron trapping by S vacancies. Ultimately, the small electron polarons reside at S vacancies, effectively extending the lifetime of carriers to 6.3 ns. Figure 7(f) schematically outlines the processes of electron and hole polaron generation in the CdS single crystal. This study provides direct experimental evidence for the formation of hole polarons.

3. CONCLUSIONS AND OUTLOOK

The current Featured Article highlights the application of TIRA–EESS in probing mid-gap defect states and the capability of TAS in the detection of electron and hole polarons. Correlations between photocatalytic activity and energy levels of defect states can be established, shedding light on understanding photocatalytic redox reactions and improving the performance of photocatalytic semiconductors through defect engineering.

Specifically, TIRA–EESS offers enhanced energy resolution for detecting defect energy levels within bandgap of TiO₂, ZnO, and CdS, enabling the observation of numerous discrete energy levels. It permits the accurate characterization of both the initial and final states of electron excitation, facilitating the determination of the Fermi level of trapped electrons. The results contribute to proposing structural models for defect states within the band gaps of several semiconductor materials, such as anatase and rutile TiO₂, ZnO, and CdS. Based on the results of TAS, we have identified the formation of electron and hole polarons at specific defect sites.

We propose several aspects for future study to overcome current limitations in TAS:

- I. Spatial resolution of defects: The limited spatial resolution of time-resolved TAS hinders the measurement of spatially resolved spectra and kinetics, both at the surface and inside the bulk, restricting its applicability in studying anisotropy and migration of free carriers and polarons. Therefore, combining femtosecond time resolution spectroscopy with spatial resolution microscopes, such as polarized Raman spectroscopy,¹³⁸ ultrafast electron diffuse scattering,¹³⁹ and scattering-type scanning near-field optical microscopy,¹⁴⁰ holds promise for providing comprehensive temporal and spatial information.
- II. Structural and spin resolution of defects: Polarons located at defect states play crucial roles in carrier localization and charge recombination, often influencing photocatalytic activity negatively. However, observations in ZnO and CdS reveal that polarons exhibit prolonged lifetimes compared to free carriers,^{32,112} suggesting potential benefits for photocatalytic efficiency. This prolonged lifetime may arise from spin interactions of trapped carriers with their local environment.¹⁴¹ Further efforts are necessary to investigate these spin-interaction mechanisms.
- III. In situ detection of photophysical properties of photocatalytic semiconductors: Genuine chemical reactions and complicated environmental conditions can markedly alter the properties of the semiconductor surface, such as the energy levels of defect states and the direction of carrier transfer. However, most photophysical properties studied via TAS were conducted only under laser irradiation, without incorporating chemical reactions on semiconductors. Hence, studying the ultrafast process of

semiconductors under real chemical reaction conditions may offer practical insights for applications.

AUTHOR INFORMATION

Corresponding Author

Yuxiang Weng – Laboratory of Soft Matter Physics, Beijing National Laboratory for Condensed Matter Physics, Institute of Physics, Chinese Academy of Sciences, Beijing 100190, China; School of Physical Sciences, University of Chinese Academy of Sciences, Beijing 100049, China; Songshan Lake Materials Laboratory, Dongguan, Guangdong 523808, China; orcid.org/0000-0003-0423-2266; Email: yxweng@iphy.ac.cn

Authors

YanJun Xu – Laboratory of Soft Matter Physics, Beijing National Laboratory for Condensed Matter Physics, Institute of Physics, Chinese Academy of Sciences, Beijing 100190, China; School of Physical Sciences, University of Chinese Academy of Sciences, Beijing 100049, China; orcid.org/0009-0005-2261-1499

Zhuan Wang – Laboratory of Soft Matter Physics, Beijing National Laboratory for Condensed Matter Physics, Institute of Physics, Chinese Academy of Sciences, Beijing 100190, China; Songshan Lake Materials Laboratory, Dongguan, Guangdong 523808, China

Complete contact information is available at:
<https://pubs.acs.org/10.1021/acs.jpcc.4c03688>

Notes

The authors declare no competing financial interest.

Biographies



YanJun Xu is currently pursuing a Ph.D. in optics at the Institute of Physics, CAS, under the guidance of Professor Yuxiang Weng. She received her Bachelor's degree in 2019 from China University of Petroleum (East China). Her research is centered on the TA spectrum of photocatalytic semiconductors, specifically focusing on the dynamics of excited carriers in defect states and polarons.



Zhuan Wang serves as an Associate Professor at the Institute of Physics, CAS. She received her Bachelor's and Ph.D. degrees in optics from Tianjin University (1996–2005). Between 2005 and 2009, she held postdoctoral positions in Physics at the University of Tokyo and the University of Electro-Communications in Japan. Her research interests involve exploring the dynamic properties of photogenerated charges in photocatalytic materials using time-resolved spectroscopy.



Yuxiang Weng, a Professor at the Institute of Physics in China. He received his Bachelor's and Master's degrees from the Department of Chemistry at East China Normal University in 1985 and 1988, respectively. In 1993, he earned his Ph.D. in optics from the Institute of Physics in China. He conducted postdoctoral research from 1994 to 1999 at the University of Hong Kong and Emory University in the United States. Currently, Professor Weng's research focuses on time-resolved spectroscopic study of photogenerated carriers in artificial photosynthetic systems, coherent energy transfer in photosynthetic systems, and protein dynamic structure in regulation of its function. He has led the construction of femtosecond TAS, femtosecond fluorescence noncollinear optical parametric amplification spectroscopy, femtosecond two-dimensional electron spectroscopy, and a number of other time-resolved spectroscopic equipment.

ACKNOWLEDGMENTS

This work was financially supported by the National Key Research and Development Program of China (2023YFA1507001).

REFERENCES

- (1) Avcioglu, C.; Avcioglu, S.; Bekheet, M. F.; Gurlo, A. Photocatalytic Overall Water Splitting by SrTiO₃: Progress Report and Design Strategies. *ACS Appl. Energy Mater.* **2023**, *6*, 1134–1154.
- (2) Koe, W. S.; Lee, J. W.; Chong, W. C.; Pang, Y. L.; Sim, L. C. An Overview of Photocatalytic Degradation: Photocatalysts, Mechanisms, and Development of Photocatalytic Membrane. *Environ. Sci. Pollut. Res.* **2020**, *27*, 2522–2565.
- (3) Wu, C.; Corrigan, N.; Lim, C.-H.; Liu, W.; Miyake, G.; Boyer, C. Rational Design of Photocatalysts for Controlled Polymerization: Effect of Structures on Photocatalytic Activities. *Chem. Rev.* **2022**, *122*, 5476–5518.
- (4) Zhang, J.; Toe, C. Y.; Kumar, P.; Scott, J.; Amal, R. Engineering Defects in TiO₂ for the Simultaneous Production of Hydrogen and Organic Products. *Appl. Catal., B* **2023**, *333*, 122765.
- (5) Yang, Y.; Si, W.; Peng, Y.; Chen, J.; Wang, Y.; Zhou, B.; Li, J. Surface Defect Engineering on Constructing High-Performance Noble Metal Active Sites: A Simple and Cost-Effective Path to High-Performance Oxidation Catalysts. *ACS Catal.* **2023**, *13*, 14792–14801.
- (6) Zhang, L.; Cheng, H.; Zong, R.; Zhu, Y. Photocorrosion Suppression of ZnO Nanoparticles Via Hybridization with Graphite-Like Carbon and Enhanced Photocatalytic Activity. *J. Phys. Chem. C* **2009**, *113*, 2368–2374.
- (7) Han, S.; Hu, L.; Gao, N.; Al-Ghamdi, A. A.; Fang, X. Efficient Self-Assembly Synthesis of Uniform CdS Spherical Nanoparticles-Au Nanoparticles Hybrids with Enhanced Photoactivity. *Adv. Funct. Mater.* **2014**, *24*, 3725–3733.
- (8) Cheng, C.; Long, R. Charge-Compensated Doping Extends Carrier Lifetimes in SrTiO₃ by Passivating Oxygen Vacancy Defects. *J. Phys. Chem. Lett.* **2021**, *12*, 12040–12047.
- (9) Xia, P.; Antonietti, M.; Zhu, B.; Heil, T.; Yu, J.; Cao, S. Designing Defective Crystalline Carbon Nitride to Enable Selective CO₂ Photoreduction in the Gas Phase. *Adv. Funct. Mater.* **2019**, *29*, 1900093.
- (10) Chen, J.; Kang, N.; Fan, J.; Lu, C.; Lv, K. Carbon Nitride for Photocatalytic Water Splitting to Produce Hydrogen and Hydrogen Peroxide. *Mater. Today Chem.* **2022**, *26*, 101028.
- (11) Shahrezaei, M.; Hejazi, S. M. H.; Kmentova, H.; Sedajova, V.; Zboril, R.; Naldoni, A.; Kment, S. Ultrasound-Driven Defect Engineering in TiO_{2-x} Nanotubes—toward Highly Efficient Platinum Single Atom-Enhanced Photocatalytic Water Splitting. *ACS Appl. Mater. Interfaces* **2023**, *15*, 37976–37985.
- (12) Pei, Z.; Ding, L.; Hu, J.; Weng, S.; Zheng, Z.; Huang, M.; Liu, P. Defect and its Dominance in ZnO Films: A New Insight into the Role of Defect over Photocatalytic Activity. *Appl. Catal., B* **2013**, *142–143*, 736–743.
- (13) Shi, R.; Ye, H.-F.; Liang, F.; Wang, Z.; Li, K.; Weng, Y.; Lin, Z.; Fu, W.-F.; Che, C.-M.; Chen, Y. Interstitial P-Doped CdS with Long-Lived Photogenerated Electrons for Photocatalytic Water Splitting without Sacrificial Agents. *Adv. Mater.* **2018**, *30*, 1705941.
- (14) Pastor, E.; Sachs, M.; Selim, S.; Durrant, J. R.; Bakulin, A. A.; Walsh, A. Electronic Defects in Metal Oxide Photocatalysts. *Nat. Rev. Mater.* **2022**, *7*, 503–521.
- (15) Maarisetty, D.; Baral, S. S. Defect Engineering in Photocatalysis: Formation, Chemistry, Optoelectronics, and Interface Studies. *J. Mater. Chem. A* **2020**, *8*, 18560–18604.
- (16) Zhang, N.; Gao, C.; Xiong, Y. Defect Engineering: A Versatile Tool for Tuning the Activation of Key Molecules in Photocatalytic Reactions. *J. Energy Chem.* **2019**, *37*, 43–57.
- (17) Liccardo, L.; Bordin, M.; Sheverdyeva, P. M.; Belli, M.; Moras, P.; Vomiero, A.; Moretti, E. Surface Defect Engineering in Colored TiO₂ Hollow Spheres toward Efficient Photocatalysis. *Adv. Funct. Mater.* **2023**, *33*, 2212486.
- (18) Zhang, D.; Dong, S. Challenges in Band Alignment between Semiconducting Materials: A Case of Rutile and Anatase TiO₂. *Prog. Nat. Sci.* **2019**, *29*, 277–284.
- (19) Walter, M. G.; Warren, E. L.; McKone, J. R.; Boettcher, S. W.; Mi, Q.; Santori, E. A.; Lewis, N. S. Solar Water Splitting Cells. *Chem. Rev.* **2010**, *110*, 6446–6473.
- (20) Corby, S.; Rao, R. R.; Steier, L.; Durrant, J. R. The Kinetics of Metal Oxide Photoanodes from Charge Generation to Catalysis. *Nat. Rev. Mater.* **2021**, *6*, 1136–1155.
- (21) Emin, D. Optical Properties of Large and Small Polarons and Bipolarons. *Phys. Rev. B* **1993**, *48*, 13691–13702.
- (22) Zhu, D.; Sun, Y.; Yuan, S.; Gao, R.; Wang, Y.; Ai, X.-C.; Zhang, J.-P. Intrapap State Engineering for Tunable Single-Photon Upconversion

Photoluminescence of Lead Halide Perovskite. *J. Phys. Chem. C* **2022**, *126*, 2447–2453.

(23) Wang, X.; Sun, Y.; Wang, Y.; Ai, X.-C.; Zhang, J.-P. Lewis Base Plays a Double-Edged-Sword Role in Trap State Engineering of Perovskite Polycrystals. *J. Phys. Chem. Lett.* **2022**, *13*, 1571–1577.

(24) Brüninghoff, R.; Wenderich, K.; Korterik, J. P.; Mei, B. T.; Mul, G.; Huijser, A. Time-Dependent Photoluminescence of Nanostructured Anatase TiO₂ and the Role of Bulk and Surface Processes. *J. Phys. Chem. C* **2019**, *123*, 26653–26661.

(25) Hossain, M. T.; Jena, T.; Debnath, S.; Giri, P. K. Defect-Induced Photogating Effect and its Modulation in Ultrathin Free-Standing Bi₂O₃ Nanosheets with a Visible-to-near-Infrared Photoresponse. *J. Mater. Chem. C* **2023**, *11*, 6670–6684.

(26) Liang, X.; Guo, Y.; Yuan, S.; Zhu, D.; Wang, Y.; Qin, Y.; Zhang, J.-P.; Ai, X.-C. Simultaneous Transport Promotion and Recombination Suppression in Perovskite Solar Cells by Defect Passivation with Li-Doped Graphitic Carbon Nitride. *J. Phys. Chem. C* **2021**, *125*, 5525–5533.

(27) Park, S. H.; Katoch, A.; Chae, K. H.; Gautam, S.; Miedema, P.; Cho, S. W.; Kim, M.; Wang, R.-P.; Lazemi, M.; de Groot, F.; et al. Direct and Real-Time Observation of Hole Transport Dynamics in Anatase TiO₂ Using X-Ray Free-Electron Laser. *Nat. Commun.* **2022**, *13*, 2531.

(28) Rittmann-Frank, M. H.; Milne, C. J.; Rittmann, J.; Reinhard, M.; Penfold, T. J.; Chergui, M. Mapping of the Photoinduced Electron Traps in TiO₂ by Picosecond X-Ray Absorption Spectroscopy. *Angew. Chem., Int. Ed.* **2014**, *53*, 5858–5862.

(29) Das, S.; Rakshit, S.; Datta, A. Interplay of Multiexciton Relaxation and Carrier Trapping in Photoluminescent CdS Quantum Dots Prepared in Aqueous Medium. *J. Phys. Chem. C* **2020**, *124*, 28313–28322.

(30) Zhu, M.; Mi, Y.; Zhu, G.; Li, D.; Wang, Y.; Weng, Y. Determination of Midgap State Energy Levels of an Anatase TiO₂ Nanocrystal Film by Nanosecond Transient Infrared Absorption - Excitation Energy Scanning Spectra. *J. Phys. Chem. C* **2013**, *117*, 18863–18869.

(31) Mi, Y.; Weng, Y. Band Alignment and Controllable Electron Migration between Rutile and Anatase TiO₂. *Sci. Rep.* **2015**, *5*, 11482.

(32) Xu, Y.; Wang, Z.; Chen, H.; Weng, Y. Photoexcited Electron and Hole Polaron Formation in CdS Single Crystals Revealed by Femtosecond Time-Resolved IR Spectroscopy. *J. Phys. Chem. C* **2024**, *128*, 2096–2106.

(33) Elahifard, M.; Sadrian, M. R.; Mirzanejad, A.; Behjatmanesh-Ardakani, R.; Ahmadvand, S. Dispersion of Defects in TiO₂ Semiconductor: Oxygen Vacancies in the Bulk and Surface of Rutile and Anatase. *Catalysts* **2020**, *10*, 397.

(34) Hao, Y.-n.; Chen, T.; Zhang, X.; Zhou, H.; Ma, Y. Ti-Ti Σ Bond at Oxygen Vacancy Inducing the Deep Defect Level in Anatase TiO₂ (101) Surface. *J. Chem. Phys.* **2019**, *150*, 224702.

(35) Naldoni, A.; Allietta, M.; Santangelo, S.; Marelli, M.; Fabbri, F.; Cappelli, S.; Bianchi, C. L.; Psaro, R.; Dal Santo, V. Effect of Nature and Location of Defects on Bandgap Narrowing in Black TiO₂ Nanoparticles. *J. Am. Chem. Soc.* **2012**, *134*, 7600–7603.

(36) Pallotti, D. K.; Passoni, L.; Maddalena, P.; Di Fonzo, F.; Lettieri, S. Photoluminescence Mechanisms in Anatase and Rutile TiO₂. *J. Phys. Chem. C* **2017**, *121*, 9011–9021.

(37) Janotti, A.; Varley, J. B.; Rinke, P.; Umezawa, N.; Kresse, G.; Van de Walle, C. G. Hybrid Functional Studies of the Oxygen Vacancy in TiO₂. *Phys. Rev. B* **2010**, *81*, 085212.

(38) Janotti, A.; Van de Walle, C. G. Oxygen Vacancies in ZnO. *Appl. Phys. Lett.* **2005**, *87*, 122102.

(39) Tauc, J.; Mentel, A. States in the Gap. *J. Non-Cryst. Solids* **1972**, *8–10*, 569–585.

(40) Wu, J.; Zheng, J.; Wu, P.; Xu, R. Study of Native Defects and Transition-Metal (Mn, Fe, Co, and Ni) Doping in a Zinc-Blende CdS Photocatalyst by DFT and Hybrid DFT Calculations. *J. Phys. Chem. C* **2011**, *115*, 5675–5682.

(41) Lany, S.; Zunger, A. Anion Vacancies as a Source of Persistent Photoconductivity in II-VI and Chalcopyrite Semiconductors. *Phys. Rev. B* **2005**, *72*, 035215.

(42) Nishidate, K.; Sato, T.; Matsukura, Y.; Baba, M.; Hasegawa, M.; Sasaki, T. Density-Functional Electronic Structure Calculations for Native Defects and Cu Impurities in CdS. *Phys. Rev. B* **2006**, *74*, 035210.

(43) Morgan, B. J.; Watson, G. W. Polaronic Trapping of Electrons and Holes by Native Defects in Anatase TiO₂. *Phys. Rev. B* **2009**, *80*, 233102.

(44) Guo, D.; Qiu, C.; Yang, K.; Deng, H.-X. Nonradiative Carrier Recombination Enhanced by Vacancy Defects in Ionic II-VI Semiconductors. *Phys. Rev. Appl.* **2021**, *15*, 064025.

(45) Mora-Seró, I.; Bisquert, J. Fermi Level of Surface States in TiO₂ Nanoparticles. *Nano Lett.* **2003**, *3*, 945–949.

(46) Shalish, I. Effect of Van Hove Singularities on the Photovoltage Spectra of Semiconductors. *Phys. Rev. B* **2002**, *66*, 165214.

(47) Franchini, C.; Reticcioli, M.; Setvin, M.; Diebold, U. Polarons in Materials. *Nat. Rev. Mater.* **2021**, *6*, 560–586.

(48) Landau, L. D. Über Die Bewegung Der Elektronen in Kristallgitter. *Phys. Z. Soviet.* **1933**, *3*, 664.

(49) Landau, L. D. The Movement of Electrons in the Crystal Lattice. *Phys. Z. Sowjetunion* **1933**, *3*, 644–645.

(50) Hupfer, A.; Vines, L.; Monakhov, E. V.; Svensson, B. G.; Herklotz, F. Photoinduced Small Polarons Bound to Hydrogen Defects in Rutile TiO₂. *Phys. Rev. B* **2017**, *96*, 085203.

(51) Fröhlich, H.; Pelzer, H.; Zienau, S. Properties of Slow Electrons in Polar Materials. *London Edinb. Dublin philos. mag. j. sci.* **1950**, *41*, 221–242.

(52) Frederikse, H. P. R. Recent Studies on Rutile (TiO₂). *J. Appl. Phys.* **1961**, *32*, 2211–2215.

(53) Janotti, A.; Franchini, C.; Varley, J. B.; Kresse, G.; Van de Walle, C. G. Dual Behavior of Excess Electrons in Rutile TiO₂. *Phys. Status Solidi Rapid Res. Lett.* **2013**, *7*, 199–203.

(54) Sezen, H.; Buchholz, M.; Nefedov, A.; Natzeck, C.; Heissler, S.; Di Valentin, C.; Wöll, C. Probing Electrons in TiO₂ Polaronic Trap States by IR-Absorption: Evidence for the Existence of Hydrogenic States. *Sci. Rep.* **2014**, *4*, 3808.

(55) Sio, W. H.; Verdi, C.; Poncé, S.; Giustino, F. Polarons from First Principles, without Supercells. *Phys. Rev. Lett.* **2019**, *122*, 246403.

(56) Holstein, T. Studies of Polaron Motion: Part I. The Molecular-Crystal Model. *Ann. Phys. (N Y)* **1959**, *8*, 325–342.

(57) Holstein, T. Studies of Polaron Motion: Part II. The “Small” Polaron. *Ann. Phys. (N Y)* **1959**, *8*, 343–389.

(58) Deskins, N. A.; Dupuis, M. Electron Transport Via Polaron Hopping in Bulk TiO₂: A Density Functional Theory Characterization. *Phys. Rev. B* **2007**, *75*, 195212.

(59) Emin, D. Small Polarons. *Phys. Today* **1982**, *35*, 34–40.

(60) Lee, H.; Poncé, S.; Bushick, K.; Hajinazar, S.; Lafuente-Bartolome, J.; Leveille, J.; Lian, C.; Lihm, J.-M.; Macheda, F.; Mori, H.; et al. Electron-Phonon Physics from First Principles Using the Epw Code. *NPJ. Comput. Mater.* **2023**, *9*, 156.

(61) Natanzon, Y.; Azulay, A.; Amouyal, Y. Evaluation of Polaron Transport in Solids from First-Principles. *Isr. J. Chem.* **2020**, *60*, 768–786.

(62) Di Valentin, C.; Pacchioni, G.; Selloni, A. Electronic Structure of Defect States in Hydroxylated and Reduced Rutile TiO₂(110) Surfaces. *Phys. Rev. Lett.* **2006**, *97*, 166803.

(63) Zhu, H.; Yang, Q.; Liu, D.; Liu, D.; Zhang, W.; Chu, Z.; Wang, X.; Yan, S.; Li, Z.; Zou, Z. Polaron States as a Massive Electron-Transfer Pathway at Heterojunction Interface. *J. Phys. Chem. Lett.* **2020**, *11*, 9184–9194.

(64) Zhu, H.; Xiao, S.; Tu, W.; Yan, S.; He, T.; Zhu, X.; Yao, Y.; Zhou, Y.; Zou, Z. In Situ Determination of Polaron-Mediated Ultrafast Electron Trapping in Rutile TiO₂ Nanorod Photoanodes. *J. Phys. Chem. Lett.* **2021**, *12*, 10815–10822.

(65) Panayotov, D. A.; Burrows, S. P.; Morris, J. R. Infrared Spectroscopic Studies of Conduction Band and Trapped Electrons in UV-Photoexcited, H-Atom N-Doped, and Thermally Reduced TiO₂. *J. Phys. Chem. C* **2012**, *116*, 4535–4544.

(66) Hruska, E.; Husek, J.; Bandaranayake, S.; Baker, L. R. Visible Light Absorption and Hot Carrier Trapping in Anatase TiO₂: The Role

- of Surface Oxygen Vacancies. *J. Phys. Chem. C* **2022**, *126*, 10752–10761.
- (67) Reticcioli, M.; Setvin, M.; Hao, X.; Flauger, P.; Kresse, G.; Schmid, M.; Diebold, U.; Franchini, C. Polaron-Driven Surface Reconstructions. *Phys. Rev. X* **2017**, *7*, 031053.
- (68) Yim, C. M.; Chen, J.; Zhang, Y.; Shaw, B.-J.; Pang, C. L.; Grinter, D. C.; Bluhm, H.; Salmeron, M.; Muryu, C. A.; Michaelides, A.; et al. Visualization of Water-Induced Surface Segregation of Polarons on Rutile TiO₂(110). *J. Phys. Chem. Lett.* **2018**, *9*, 4865–4871.
- (69) Patera, L. L.; Queck, F.; Scheuerer, P.; Repp, J. Mapping Orbital Changes Upon Electron Transfer with Tunnelling Microscopy on Insulators. *Nature* **2019**, *566*, 245–248.
- (70) Moser, S.; Moreschini, L.; Jaćimović, J.; Barišić, O. S.; Berger, H.; Magrez, A.; Chang, Y. J.; Kim, K. S.; Bostwick, A.; Rotenberg, E.; et al. Tunable Polaronic Conduction in Anatase TiO₂. *Phys. Rev. Lett.* **2013**, *110*, 196403.
- (71) Kispert, L. D.; Joseph, J.; Miller, G. G.; Baughman, R. H. EPR Study of Polarons in a Conducting Polymer with Nondegenerate Ground States: Alkali Metal Complexes of Poly (P Phenylene) and Phenylene Oligomers. *J. Chem. Phys.* **1984**, *81*, 2119–2125.
- (72) Yang, S.; Brant, A. T.; Giles, N. C.; Halliburton, L. E. Intrinsic Small Polarons in Rutile TiO₂. *Phys. Rev. B* **2013**, *87*, 125201.
- (73) Di Valentin, C.; Finazzi, E.; Pacchioni, G.; Selloni, A.; Livraghi, S.; Czoska, A. M.; Paganini, M. C.; Giamello, E. Density Functional Theory and Electron Paramagnetic Resonance Study on the Effect of N-F Codoping of TiO₂. *Chem. Mater.* **2008**, *20*, 3706–3714.
- (74) Roy, P.; Anandan, G. T.; Nayak, N.; Kumar, A.; Dasgupta, J. Raman Snapshots of Side-Chain Dependent Polaron Dynamics in Polythiophene Films. *J. Phys. Chem. B* **2023**, *127*, 567–576.
- (75) Yoon, S.; Liu, H. L.; Schollerer, G.; Cooper, S. L.; Han, P. D.; Payne, D. A.; Cheong, S. W.; Fisk, Z. Raman and Optical Spectroscopic Studies of Small-to-Large Polaron Crossover in the Perovskite Manganese Oxides. *Phys. Rev. B* **1998**, *58*, 2795–2801.
- (76) Kurus, N. N.; Milekhin, A. G.; Sklyar, R. I.; Saidzhonov, B. M.; Vasiliev, R. B.; Adichtchev, S. V.; Surovtsev, N. V.; Latyshev, A. V.; Zahn, D. R. T. Phonons in Core-Shell CdSe/CdS Nanoplatelets Studied by Vibrational Spectroscopies. *J. Phys. Chem. C* **2022**, *126*, 7107–7116.
- (77) Guo, C.; Meng, X.; Fu, H.; Wang, Q.; Wang, H.; Tian, Y.; Peng, J.; Ma, R.; Weng, Y.; Meng, S.; et al. Probing Nonequilibrium Dynamics of Photoexcited Polarons on a Metal-Oxide Surface with Atomic Precision. *Phys. Rev. Lett.* **2020**, *124*, 206801.
- (78) Ohta, K.; Tominaga, K.; Ikoma, T.; Kobori, Y.; Yamada, H. Microscopic Structures, Dynamics, and Spin Configuration of the Charge Carriers in Organic Photovoltaic Solar Cells Studied by Advanced Time-Resolved Spectroscopic Methods. *Langmuir* **2022**, *38*, 7365–7382.
- (79) Jin, W.; Kim, H. H.; Ye, Z.; Ye, G.; Rojas, L.; Luo, X.; Yang, B.; Yin, F.; Horng, J. S. A.; Tian, S.; et al. Observation of the Polaronic Character of Excitons in a Two-Dimensional Semiconducting Magnet CrI₃. *Nat. Commun.* **2020**, *11*, 4780.
- (80) Piercy, V. L.; Saeed, K. H.; Prentice, A. W.; Neri, G.; Li, C.; Gardner, A. M.; Bai, Y.; Sprick, R. S.; Sazanovich, I. V.; Cooper, A. I.; et al. Time-Resolved Raman Spectroscopy of Polaron Formation in a Polymer Photocatalyst. *J. Phys. Chem. Lett.* **2021**, *12*, 10899–10905.
- (81) Chen, X.; Zhang, S.; Wang, L.; Huang, Y.-F.; Liu, H.; Huang, J.; Dong, N.; Liu, W.; Kislyakov, I. M.; Nunzi, J. M.; et al. Direct Observation of Interlayer Coherent Acoustic Phonon Dynamics in Bilayer and Few-Layer PtSe₂. *Photonics Res.* **2019**, *7*, 1416–1424.
- (82) Park, M.; Neukirch, A. J.; Reyes-Lillo, S. E.; Lai, M.; Ellis, S. R.; Dietze, D.; Neaton, J. B.; Yang, P.; Tretiak, S.; Mathies, R. A. Excited-State Vibrational Dynamics toward the Polaron in Methylammonium Lead Iodide Perovskite. *Nat. Commun.* **2018**, *9*, 2525.
- (83) Pastor, E.; Park, J.-S.; Steier, L.; Kim, S.; Grätzel, M.; Durrant, J. R.; Walsh, A.; Bakulin, A. A. In Situ Observation of Picosecond Polaron Self-Localisation in α -Fe₂O₃ Photoelectrochemical Cells. *Nat. Commun.* **2019**, *10*, 3962.
- (84) Dong, S.; Lian, J.; Jhon, M. H.; Chan, Y.; Loh, Z.-H. Pump-Power Dependence of Coherent Acoustic Phonon Frequencies in Colloidal CdSe/CdS Core/Shell Nanoplatelets. *Nano Lett.* **2017**, *17*, 3312–3319.
- (85) Yamakata, A.; Ishibashi, T.-a.; Onishi, H. Kinetics of the Photocatalytic Water-Splitting Reaction on TiO₂ and Pt/TiO₂ Studied by Time-Resolved Infrared Absorption Spectroscopy. *J. Mol. Catal. A: Chem.* **2003**, *199*, 85–94.
- (86) Zhao, H.; Zhang, Q.; Weng, Y.-X. Deep Surface Trap Filling by Photoinduced Carriers and Interparticle Electron Transport Observed in TiO₂ Nanocrystalline Film with Time-Resolved Visible and Mid-IR Transient Spectroscopies. *J. Phys. Chem. C* **2007**, *111*, 3762–3769.
- (87) Smith, R. A. *Semiconductors*; Cambridge University Press: Cambridge, U.K., 1978.
- (88) Zhao, H.; Pan, F.; Li, Y. A Review on the Effects of TiO₂ Surface Point Defects on CO₂ Photoreduction with H₂O. *J. Materiomics* **2017**, *3*, 17–32.
- (89) Hinuma, Y.; Toyao, T.; Kamachi, T.; Maeno, Z.; Takakusagi, S.; Furukawa, S.; Takigawa, I.; Shimizu, K.-i. Density Functional Theory Calculations of Oxygen Vacancy Formation and Subsequent Molecular Adsorption on Oxide Surfaces. *J. Phys. Chem. C* **2018**, *122*, 29435–29444.
- (90) Li, Y.-F.; Aschauer, U.; Chen, J.; Selloni, A. Adsorption and Reactions of O₂ on Anatase TiO₂. *Acc. Chem. Res.* **2014**, *47*, 3361–3368.
- (91) Li, J.; Zhang, M.; Guan, Z.; Li, Q.; He, C.; Yang, J. Synergistic Effect of Surface and Bulk Single-Electron-Trapped Oxygen Vacancy of TiO₂ in the Photocatalytic Reduction of CO₂. *Appl. Catal., B* **2017**, *206*, 300–307.
- (92) Wu, T.; Zhao, H.; Zhu, X.; Xing, Z.; Liu, Q.; Liu, T.; Gao, S.; Lu, S.; Chen, G.; Asiri, A. M.; et al. Identifying the Origin of Ti³⁺ Activity toward Enhanced Electrocatalytic N₂ Reduction over TiO₂ Nanoparticles Modulated by Mixed-Valent Copper. *Adv. Mater.* **2020**, *32*, 2000299.
- (93) Gao, Y.; Zhu, J.; An, H.; Yan, P.; Huang, B.; Chen, R.; Fan, F.; Li, C. Directly Probing Charge Separation at Interface of TiO₂ Phase Junction. *J. Phys. Chem. Lett.* **2017**, *8*, 1419–1423.
- (94) Abdullah, S. A.; Sahdan, M. Z.; Nafarizal, N.; Saim, H.; Bakri, A. S.; Cik Rohaida, C. H.; Adriyanto, F.; Sari, Y. Photoluminescence Study of Trap-State Defect on TiO₂ Thin Films at Different Substrate Temperature Via Rf Magnetron Sputtering. *J. Phys. Conf. Ser.* **2018**, *995*, 012067.
- (95) Nowotny, J.; Alim, M. A.; Bak, T.; Idris, M. A.; Ionescu, M.; Prince, K.; Sahdan, M. Z.; Sopian, K.; Mat Teridi, M. A.; Sigmund, W. Defect Chemistry and Defect Engineering of TiO₂-Based Semiconductors for Solar Energy Conversion. *Chem. Soc. Rev.* **2015**, *44*, 8424–8442.
- (96) Bak, T.; Nowotny, J.; Sucher, N. J.; Wachsman, E. Effect of Crystal Imperfections on Reactivity and Photoreactivity of TiO₂ (Rutile) with Oxygen, Water, and Bacteria. *J. Phys. Chem. C* **2011**, *115*, 15711–15738.
- (97) He, J.; Behera, R. K.; Finnis, M. W.; Li, X.; Dickey, E. C.; Phillipot, S. R.; Sinnott, S. B. Prediction of High-Temperature Point Defect Formation in TiO₂ from Combined Ab Initio and Thermodynamic Calculations. *Acta Mater.* **2007**, *55*, 4325–4337.
- (98) Wang, S.; Pan, L.; Song, J.-J.; Mi, W.; Zou, J.-J.; Wang, L.; Zhang, X. Titanium-Defected Undoped Anatase TiO₂ with P-Type Conductivity, Room-Temperature Ferromagnetism, and Remarkable Photocatalytic Performance. *J. Am. Chem. Soc.* **2015**, *137*, 2975–2983.
- (99) Di Valentin, C.; Selloni, A. Bulk and Surface Polarons in Photoexcited Anatase TiO₂. *J. Phys. Chem. Lett.* **2011**, *2*, 2223–2228.
- (100) Li, R.; Weng, Y.; Zhou, X.; Wang, X.; Mi, Y.; Chong, R.; Han, H.; Li, C. Achieving Overall Water Splitting Using Titanium Dioxide-Based Photocatalysts of Different Phases. *Energy Environ. Sci.* **2015**, *8*, 2377–2382.
- (101) Du, Y.; Wang, Z.; Chen, H.; Wang, H.-Y.; Liu, G.; Weng, Y. Effect of Trap States on Photocatalytic Properties of Boron-Doped Anatase TiO₂ Microspheres Studied by Time-Resolved Infrared Spectroscopy. *Phys. Chem. Chem. Phys.* **2019**, *21*, 4349–4358.

- (102) Liu, Q. Ultrafast Time-Resolved Spectroscopy of Zinc Oxide Based Semiconductor Photocatalysts. Ph.D. Dissertation, Institute of Physics, Chinese Academy of Science, 2021.
- (103) Sharma, D. K.; Shukla, S.; Sharma, K. K.; Kumar, V. A Review on ZnO: Fundamental Properties and Applications. *Mater. Today: Proc.* **2022**, *49*, 3028–3035.
- (104) Wang, W.; Li, K.; Lan, J.; Shen, M.; Wang, Z.; Feng, X.; Yu, H.; Chen, K.; Li, J.; Zhou, F.; et al. Cmos Backend-of-Line Compatible Memory Array and Logic Circuitries Enabled by High Performance Atomic Layer Deposited ZnO Thin-Film Transistor. *Nat. Commun.* **2023**, *14*, 6079.
- (105) Klüpfel, F. J.; von Wenckstern, H.; Grundmann, M. Ring Oscillators Based on ZnO Channel Jfets and Mesfets. *Adv. Electron. Mater.* **2016**, *2*, 1500431.
- (106) Drmosh, Q. A.; Al Wajih, Y. A.; Alade, I. O.; Mohamedkhair, A. K.; Qamar, M.; Hakeem, A. S.; Yamani, Z. H. Engineering the Depletion Layer of Au-Modified ZnO/Ag Core-Shell Films for High-Performance Acetone Gas Sensing. *Sens. Actuators B Chem.* **2021**, *338*, 129851.
- (107) Tao, P.; Guo, W.; Du, J.; Tao, C.; Qing, S.; Fan, X. Continuous Wet-Process Growth of ZnO Nanoarrays for Wire-Shaped Photoanode of Dye-Sensitized Solar Cell. *J. Colloid Interface Sci.* **2016**, *478*, 172–180.
- (108) Liang, Y.-C.; Zhao, Q.; Liu, K.-K.; Liu, Q.; Lu, X.-L.; Wu, X.-Y.; Lu, Y.-J.; Dong, L.; Shan, C.-X. Ultrasensitive Mechano-Stimuli Luminescence Enhancement in ZnO Nanoparticles. *J. Phys. Chem. Lett.* **2019**, *10*, 3557–3562.
- (109) Eixenberger, J. E.; Anders, C. B.; Wada, K.; Reddy, K. M.; Brown, R. J.; Moreno-Ramirez, J.; Weltner, A. E.; Karthik, C.; Tenne, D. A.; Fologea, D.; et al. Defect Engineering of ZnO Nanoparticles for Bioimaging Applications. *ACS Appl. Mater. Interfaces* **2019**, *11*, 24933–24944.
- (110) Liu, Q.; Wang, Z.; Chen, H.; Wang, H.-Y.; Song, H.; Ye, J.; Weng, Y. Rules for Selecting Metal Cocatalyst Based on Charge Transfer and Separation Efficiency between ZnO Nanoparticles and Noble Metal Cocatalyst Ag/ Au/ Pt. *ChemCatChem* **2020**, *12*, 3838–3842.
- (111) Vaiano, V.; Jaramillo-Paez, C. A.; Matarangolo, M.; Navío, J. A.; del Carmen Hidalgo, M. UV and Visible-Light Driven Photocatalytic Removal of Caffeine Using ZnO Modified with Different Noble Metals (Pt, Ag and Au). *Mater. Res. Bull.* **2019**, *112*, 251–260.
- (112) Liu, Q.; Chen, H.; Wang, Z.; Weng, Y. Observation of the Polaron Excited State in a Single-Crystal ZnO. *J. Phys. Chem. C* **2021**, *125*, 10274–10283.
- (113) Selim, F. A.; Weber, M. H.; Solodovnikov, D.; Lynn, K. G. Nature of Native Defects in ZnO. *Phys. Rev. Lett.* **2007**, *99*, 085502.
- (114) Oba, F.; Choi, M.; Togo, A.; Tanaka, I. Point Defects in ZnO: An Approach from First Principles. *Sci. Technol. Adv. Mater.* **2011**, *12*, 034302.
- (115) Gurylev, V.; Perng, T. P. Defect Engineering of ZnO: Review on Oxygen and Zinc Vacancies. *J. Eur. Ceram. Soc.* **2021**, *41*, 4977–4996.
- (116) Penfold, T. J.; Szlachetko, J.; Santomauro, F. G.; Britz, A.; Gawelda, W.; Doumy, G.; March, A. M.; Southworth, S. H.; Rittmann, J.; Abela, R.; et al. Revealing Hole Trapping in Zinc Oxide Nanoparticles by Time-Resolved X-Ray Spectroscopy. *Nat. Commun.* **2018**, *9*, 478.
- (117) Milne, C. J.; Nagornova, N.; Pope, T.; Chen, H.-Y.; Rossi, T.; Szlachetko, J.; Gawelda, W.; Britz, A.; van Driel, T. B.; Sala, L. Disentangling the Evolution of Electrons and Holes in Photoexcited ZnO Nanoparticles. *Struct. Dyn.* **2023**, *10*, 064501.
- (118) Kumar, V.; Swart, H. C.; Ntwaeaborwa, O. M.; Kroon, R. E.; Terblans, J. J.; Shaat, S. K. K.; Yousif, A.; Duvenhage, M. M. Origin of the Red Emission in Zinc Oxide Nanophosphors. *Mater. Lett.* **2013**, *101*, 57–60.
- (119) Xie, S.; Shen, Z.; Deng, J.; Guo, P.; Zhang, Q.; Zhang, H.; Ma, C.; Jiang, Z.; Cheng, J.; Deng, D.; et al. Visible Light-Driven C-H Activation and C-C Coupling of Methanol into Ethylene Glycol. *Nat. Commun.* **2018**, *9*, 1181.
- (120) Utterback, J. K.; Grennell, A. N.; Wilker, M. B.; Pearce, O. M.; Eaves, J. D.; Dukovic, G. Observation of Trapped-Hole Diffusion on the Surfaces of CdS Nanorods. *Nat. Chem.* **2016**, *8*, 1061–1066.
- (121) Cline, R. P.; Utterback, J. K.; Strong, S. E.; Dukovic, G.; Eaves, J. D. On the Nature of Trapped-Hole States in CdS Nanocrystals and the Mechanism of Their Diffusion. *J. Phys. Chem. Lett.* **2018**, *9*, 3532–3537.
- (122) Varley, J. B.; Lordi, V. Electrical Properties of Point Defects in CdS and ZnS. *Appl. Phys. Lett.* **2013**, *103*, 102103.
- (123) Xu, X.; Zhao, Y.; Sie, E. J.; Lu, Y.; Liu, B.; Ekahana, S. A.; Ju, X.; Jiang, Q.; Wang, J.; Sun, H.; et al. Dynamics of Bound Exciton Complexes in CdS Nanobelts. *ACS Nano* **2011**, *5*, 3660–3669.
- (124) Fang, Y.; Song, J.; Zheng, R.; Zeng, Y.; Sun, J. Electrogenerated Chemiluminescence Emissions from CdS Nanoparticles for Probing of Surface Oxidation. *J. Phys. Chem. C* **2011**, *115*, 9117–9121.
- (125) Krause, M. M.; Mooney, J.; Kambhampati, P. Chemical and Thermodynamic Control of the Surface of Semiconductor Nanocrystals for Designer White Light Emitters. *ACS Nano* **2013**, *7*, 5922–5929.
- (126) Mooney, J.; Krause, M. M.; Saari, J. I.; Kambhampati, P. Challenge to the Deep-Trap Model of the Surface in Semiconductor Nanocrystals. *Phys. Rev. B* **2013**, *87*, 081201.
- (127) Tanner, A. J.; Thornton, G. TiO₂ Polarons in the Time Domain: Implications for Photocatalysis. *J. Phys. Chem. Lett.* **2022**, *13*, 559–566.
- (128) Setvin, M.; Franchini, C.; Hao, X.; Schmid, M.; Janotti, A.; Kaltak, M.; Van de Walle, C. G.; Kresse, G.; Diebold, U. Direct View at Excess Electrons in TiO₂ Rutile and Anatase. *Phys. Rev. Lett.* **2014**, *113*, 086402.
- (129) Deák, P.; Aradi, B.; Frauenheim, T. Quantitative Theory of the Oxygen Vacancy and Carrier Self-Trapping in Bulk TiO₂. *Phys. Rev. B* **2012**, *86*, 195206.
- (130) Mou, T.; Gupta, V. K.; Tabriz, M. F.; Frauenheim, T.; Deák, P. Size of Electron Polarons in Anatase TiO₂ and Their Role in Photocatalysis. *Phys. Rev. B* **2023**, *107*, 155127.
- (131) Obara, Y.; Ito, H.; Ito, T.; Kurahashi, N.; Thürmer, S.; Tanaka, H.; Katayama, T.; Togashi, T.; Owada, S.; Yamamoto, Y.-i.; et al. Femtosecond Time-Resolved X-Ray Absorption Spectroscopy of Anatase TiO₂ Nanoparticles Using Xfel. *Structural Dynamics* **2017**, *4*, 044033.
- (132) Zhang, Y.; Payne, D. T.; Pang, C. L.; Cacho, C.; Chapman, R. T.; Springate, E.; Fielding, H. H.; Thornton, G. State-Selective Dynamics of TiO₂ Charge-Carrier Trapping and Recombination. *J. Phys. Chem. Lett.* **2019**, *10*, 5265–5270.
- (133) Santomauro, F. G.; Lübcke, A.; Rittmann, J.; Baldini, E.; Ferrer, A.; Silatani, M.; Zimmermann, P.; Grübel, S.; Johnson, J. A.; Mariager, S. O.; et al. Femtosecond X-Ray Absorption Study of Electron Localization in Photoexcited Anatase TiO₂. *Sci. Rep.* **2015**, *5*, 14834.
- (134) Wang, X.; Feng, Z.; Shi, J.; Jia, G.; Shen, S.; Zhou, J.; Li, C. Trap States and Carrier Dynamics of TiO₂ Studied by Photoluminescence Spectroscopy under Weak Excitation Condition. *Phys. Chem. Chem. Phys.* **2010**, *12*, 7083–7090.
- (135) Groser, I.; Rosenzweig, M. Magneto-Brillouin Scattering of Polaritons in CdS. *Solid State Commun.* **1980**, *36*, 1027–1031.
- (136) Winterling, G.; Koteles, E. Resonant Brillouin Scattering near the a Exciton in CdS. *Solid State Commun.* **1977**, *23*, 95–98.
- (137) Yu, P. Y.; Evangelisti, F. Two-Phonon Resonant Brillouin Scattering in CdS. *Solid State Commun.* **1978**, *27*, 87–89.
- (138) Ling, X.; Huang, S.; Hasdeo, E. H.; Liang, L.; Parkin, W. M.; Tatsumi, Y.; Nugraha, A. R. T.; Puzos, A. A.; Das, P. M.; Sumpter, B. G.; et al. Anisotropic Electron-Photon and Electron-Phonon Interactions in Black Phosphorus. *Nano Lett.* **2016**, *16*, 2260–2267.
- (139) Seiler, H.; Zahn, D.; Zacharias, M.; Hildebrandt, P.-N.; Vasileiadis, T.; Windsor, Y. W.; Qi, Y.; Carbogno, C.; Draxl, C.; Ernstorfer, R.; et al. Accessing the Anisotropic Nonthermal Phonon Populations in Black Phosphorus. *Nano Lett.* **2021**, *21*, 6171–6178.
- (140) Ma, W.; Alonso-González, P.; Li, S.; Nikitin, A. Y.; Yuan, J.; Martín-Sánchez, J.; Taboada-Gutiérrez, J.; Amenabar, I.; Li, P.; Vélez, S.; et al. In-Plane Anisotropic and Ultra-Low-Loss Polaritons in a Natural Van Der Waals Crystal. *Nature* **2018**, *562*, 557–562.

(141) van Schooten, K. J.; Huang, J.; Talapin, D. V.; Boehme, C.; Lupton, J. M. Spin-Dependent Electronic Processes and Long-Lived Spin Coherence of Deep-Level Trap Sites in CdS Nanocrystals. *Phys. Rev. B* **2013**, *87*, 125412.